



CENTRO DE INVESTIGACIONES
EN ÓPTICA, A.C.

“STUDY OF THE PROPAGATION OF ENTANGLED PHOTONS IN ORBITAL ANGULAR MOMENTUM WITH LAGUERRE AND INCE-GAUSS MODES THROUGH A TURBULENT ATMOSPHERE”



Tesis que para obtener el grado de Maestro en Ciencias (Óptica)

Presenta: Daniel Rodríguez Guillén

Director de Tesis: Dr. Roberto Ramírez Alarcón

Versión Definitiva. Incluye cambios sugeridos por revisores. Vo. Bo.

*León · Guanajuato · México
Agosto de 2023*

Study of the propagation of entangled photons in Orbital Angular Momentum with Laguerre and Ince-Gauss modes through a Turbulent Atmosphere

By

DANIEL RODRÍGUEZ GUILLÉN

CENTRO DE INVESTIGACIONES EN ÓPTICA

For the degree of
MASTER OF SCIENCE (OPTICS)

AUGUST - 2023, LEÓN, GTO.

ADVISOR:
PHD. ROBERTO RAMÍREZ ALARCÓN

ABSTRACT

In free space optical communication, atmospheric turbulence is a significant challenge due to the random fluctuations in the refractive index caused by temperature variations in the atmosphere. This research focuses on the impact of atmospheric turbulence on entangled photons with Orbital Angular Momentum (OAM) using Laguerre and Helicoidal Ince Gauss modes. To measure the entanglement we use the concurrence, obtained by reconstructing the density matrix with quantum state tomography techniques.

In this work, we extend the investigation of Laguerre Gauss modes by considering non-zero radial indices, a novel approach that has not been studied in the literature. Furthermore, we studied the concurrence of Helicoidal Ince-Gauss modes against atmospheric turbulence. These modes, characterized by their ellipticity dependency and helicoidal phase, had not been extensively studied before.

Our findings reveal that modes with higher cylindrical symmetry exhibit greater resilience in preserving the entanglement against scintillation induced by turbulence. Our results also contribute to the existing knowledge by emphasizing that the effect of the turbulence on the entanglement is basis dependent.

The outcomes of this study have implications for practical applications. The observed resilience of higher cylindrical symmetry modes against turbulence-induced scintillation could be useful in free space optical communication systems. This includes applications in Quantum Key Distribution (QKD) and other secure communication protocols relying on entanglement preservation.

DEDICATION AND ACKNOWLEDGEMENTS

I want to thank Conahcyt for supporting me financially in my master's studies. Also, I want to thank Dr. Roberto Ramírez for allowing me to be part of his research group, and Dr. Laura for her support during my stay at the CIO. To my co-workers for the laboratory support. Lastly but not least important to Jhoanna for being a part of this journey, and to my family for all the support.

TABLE OF CONTENTS

	Page
List of Tables	iii
List of Figures	iii
1 Introduction	1
2 Laguerre and Ince-Gauss Beams	3
2.1 Laguerre-Gauss modes	3
2.2 Ince-Gauss modes	4
2.3 Helicoidal Ince-Gauss modes	8
3 Theory of Turbulence	10
3.1 Statistical description of atmospheric turbulence	10
3.2 Power spectra of refractive index fluctuations	11
3.3 Amplitude variations	13
4 Spontaneous Parametric Down Conversion Theory	15
4.1 Theoretical derivation of SPDC: classical regime	15
4.2 Theoretical derivation of SPDC: quantum regime	16
5 Spiral Bandwidth of SPDC	19
5.1 General amplitudes and structure of SPDC	19
6 Entangled Photons	23
6.1 Quantum Formalism	23
6.1.1 Concurrence	24
7 Numerical Simulation	26
7.1 Single-Phase Screen Method	26
7.1.1 The Paterson Theory	26
7.1.2 Analytic Concurrence	27
7.1.3 Smith and Raymer theory: Two-photon wave mechanics	29

7.2	Multiple-Phase Screen Method	33
7.2.1	Geometry and Beam propagation	33
7.2.2	Avoiding Aliasing	33
7.2.3	Vacuum Propagation	35
7.2.4	Turbulent Phase Screen Generation	36
7.2.5	Turbulent Propagation	37
7.2.6	Concurrence Calculation	38
7.3	Numerical Results	40
7.3.1	Concurrence of Laguerre-Gauss modes Through Turbulence	40
7.3.2	Concurrence of Helicoidal Ince-Gauss modes Through Turbulence	41
8	Experimental Setup	44
8.1	Digital Masks on the SLM	46
8.2	Quantum State Tomography	47
9	Results and Conclusions	50
9.1	Experimental Spiral Bandwidth	50
9.2	Experimental Concurrence of Laguerre-Gauss modes	50
9.3	Experimental Concurrence of Helicoidal Ince-Gauss modes	52
9.4	Conclusions	54
	Referencias	55

LIST OF TABLES

TABLE	Page
7.1 Table with the parameters used for the simulation.	37

LIST OF FIGURES

FIGURE	Page
2.1 Intensity and phase profile for different LG modes, with azimuthal number $l = \{1, 2, 3, 4\}$ and radial number $n = \{0, 1, 2\}$	5
2.2 Intensity and phase profile of IG modes for a fixed ellipticity of 2. In a) Even IG modes are shown. In b) Odd IG modes are shown. In c) HIG^+ modes are shown.	7
2.3 Intensity and phase profile of a $HIG_{11,6}^+$ with different values of ellipticity.	8
2.4 The upper figure shows different HIG with a fixed order $p = 8$ and different degrees $m = \{2, 4, 6, 8\}$. The intensity profiles have an ellipticity of $\varepsilon = 2$. We can observe that when ellipticity tends to zero, the OAM value converges to the corresponding m value, i.e., the OAM of the LG mode, $m = l $. In the bottom figure different HIG with a fixed degree $m = 2$ and different orders $p = \{2, 4, 6, 8\}$. The intensity profiles have an ellipticity of $\varepsilon = 2$. In the same way as the left figure, OAM values converge to $m = l $ when ellipticity tends to zero. The nomenclature of $ HIG_{p,m,\varepsilon}^+\rangle$ corresponds to positive Helicoidal Ince-Gauss with subscripts order, degree, and ellipticity, respectively.	9
5.1 Spiral Bandwidth for different values of γ . Correlation between l values are shown for $p_s = p_i = 0$	21
5.2 Spiral Bandwidth for different values of γ . Correlation between l values are shown, for $p_s = p_i = 0$	22
7.1 The concurrence against scintillation strength (ω_0/r_0) , for different OAM values and the same radial number. In the case when two photons propagate through turbulence. a) Quantum radial number $n = 0$. b) Quantum radial number $n = 1$. c) Quantum radial number $n = 3$. d) Quantum radial number $n = 5$	29
7.2 The concurrence against scintillation strength (ω_0/r_0) , for different radial number and same $ l $ value. In the case when two photons propagate through turbulence. a) OAM $ l = 1$. b) OAM $ l = 2$. c) OAM $ l = 4$. d) OAM $ l = 5$	30
7.3 The concurrence against scintillation strength (ω_0/r_0) , for different OAM values and the same radial number. In the case when two photons propagate through turbulence using TWM theory. a) Quantum radial number $n = 0$. b) Quantum radial number $n = 1$. c) Quantum radial number $n = 3$. d) Quantum radial number $n = 5$	31
7.4 The concurrence against scintillation strength (ω_0/r_0) , for different radial number and same $ l $ value. In the case when two photons propagate through turbulence using TWM theory. a) OAM $ l = 1$. b) OAM $ l = 2$. c) OAM $ l = 4$. d) OAM $ l = 5$	32
7.5 Graphical representation of the first three constraints of equation (7.22).	34

7.6	Vacuum propagation of LG mode with $l = 5, n = 5$. In a) the intensity and phase of the mode before propagation, in b) the intensity and phase of the mode after propagation.	35
7.7	Generation of turbulent phase screens. Both a) and b) are the same phase screen, the only difference is that in a) phase screen is generated without subharmonic method, and in b) phase screen is generated with subharmonic method.	36
7.8	Turbulent propagation of LG mode with $l = 5, n = 5$. In a) the intensity and phase of the mode before propagation, in b) the intensity and phase after propagation.	38
7.9	Concurrence comparison for AR, TWM, and NS. The numerical simulation has the same decay behavior as both theories. The analytical result describes a higher decay, while the TWM theory underestimates the effect of turbulence. Instead, the numerical simulation has a transition more in line with the cumulative effect of turbulence. Each point on the graph was averaged 1200 times.	41
7.10	Effect of the turbulence on modes with a radial index different to zero, our NS agrees with Paterson model, as the radial number increases, the mode has less resilience, this phenomena are more distinguishable for low values of azimuthal number. Each point on the graph was averaged 1200 times.	42
7.11	Concurrence for a representative set of HIG. The mode $p = 1, m = 1$, corresponds to a LG with $l = 1, n = 0$, for this reason, the concurrence decays identical for each ellipticity. In the case of $p = 3, m = 1, 3$ there is high resilience for low ellipticities in the case $m = 3$. For a mode with a high value of $p = 15$, and different values of $m = 1, 7, 15$ same phenomenon is observed, the low ellipticities have less resilience until $m = 7$, at this point all ellipticities present similar resilience when m increases the low ellipticities have higher resilience respect to high ellipticities. Each point in the graph was averaged 1800 times.	43
8.1	Experimental setup for a photon pair generation. A detailed description of the setup is in the text.	45
8.2	The process to generate a phase-only digital mask for the SLM.	46
8.3	The comparison of a generation of a mask without turbulence and a mask with turbulence. The effect of the turbulence is projected on the diffraction effect, as the turbulence strength increases, fewer counts in coincidence are obtained, this effect is the crosstalk of the OAM.	46
8.4	Graphical visualization of the density matrix obtained by Maximum Likelihood Estimation.	48
9.1	Comparison between theoretical spiral bandwidth and experimental spiral bandwidth. In a) the experimental correlation between OAM values agrees with the theoretical correlation. In b) we find the γ value.	51

9.2	Comparison between numerical simulation and experimental measurements for LG modes. The measurements agree with the numerical simulation. Each point was averaged 40 times.	52
9.3	Comparison between numerical simulation and experimental measurements for HIG modes. The measurements follow the same pattern as NS, and the data agree with NS. Each point was averaged 40 times.	53

INTRODUCTION

One of the most important goals in optical communication in free space is to preserve the quality and properties of the beam as it propagates, a challenge to this goal is atmospheric turbulence, which induces random variations in the beam as it propagates, degrading the information contained in it. Similarly, in quantum communication in free space, the quantity we are interested in preserving is entanglement since it is the quantity that allows quantum communication.

There are various degrees of freedom in which photons can be entangled for this purpose. Historically, polarization entanglement was the first to be used in a quantum cryptography protocol, known as BB84 [1]. For polarization entanglement the dimension in Hilbert space is two, that is, the state of a photon can be completely described by the linear combination of two linearly independent vectors, for example, horizontal and vertical polarization. Compared to the entanglement in orbital angular momentum, the dimensionality in Hilbert space is infinite, this is because the orbital angular momentum value is intrinsic to the propagated mode, and since the modes are orthogonal, they represent an infinite basis, as a consequence, the dimensionality is infinite.

In more detail, the modes with orbital angular momentum correspond to spatial modes with helical phases, for example, the Laguerre-Gauss modes, which correspond to the solution of the paraxial Helmholtz equation in cylindrical coordinates. In addition to representing an infinite basis, since they are orthogonal, there is no overlap between modes, that is, the information is not lost when these modes overlap. Due to these two characteristics, entanglement with spatial modes in orbital angular momentum has become an object of study in various areas of optical communication.

The generation of entangled photons is possible spontaneous parametric down conversion. In

this process, a higher energy photon is annihilated to generate two lower energy photons, the resulting photons are correlated to some degree of freedom due to conservation of momentum and energy. The spontaneous parametric down conversion phenomenon also allows entanglement in orbital angular momentum, as described in the more detailed chapter 6. To quantify entanglement, a quantity known as concurrence is used. The effect of atmospheric turbulence on the entangled photons degrades the entanglement, and this can be observed by obtaining the concurrence.

Therefore, studying the entanglement of photons with spatial modes with orbital angular momentum through atmospheric turbulence is not trivial, but its application to quantum communications is straightforward. Projects like QUESS (Quantum Experiments at Space Scale) [2–4] are being developed, as a consequence, it is necessary to study the entanglement decay due to atmospheric turbulence.

This work is divided in such a way that each Chapter presents the necessary bases to understand all the work presented. In Chapter 2, the Laguerre and Ince-Gauss modes and their properties in OAM are discussed. In Chapter 3 the theoretical framework for understanding atmospheric turbulence and its effect on the beams is developed. In Chapter 4 the spontaneous parametric down conversion theory is developed, which is used as a source of entangled photons in OAM. Chapter 5 discusses the probability distribution in OAM of the modes generated by spontaneous parametric down conversion, known as spiral bandwidth. In Chapter 6 the quantum formalism is discussed to understand how entanglement is quantified. In Chapter 7 the results of the literature are compared with our numerical results, to corroborate that our results are valid, and extend the analysis to Laguerre Gauss modes with a radial index different from zero, and Ince-Gauss Helicoid modes. In Chapter 8 the experimental setup and the necessary considerations to make the measurements properly are discussed. Finally, in Chapter 9, the numerical and experimental results obtained throughout this study and the respective conclusions are presented.

LAGUERRE AND INCE-GAUSS BEAMS

The usual starting point for the derivation of laser beam propagation modes is solving the scalar Helmholtz equation in the paraxial approximation [5]. According to the chosen basis, one can obtain different mode solutions, for instance, choosing a cylindrical basis one obtains Laguerre-Gauss (LG) modes [5, 6], while by using a cartesian basis one gets Hermite-Gauss (HG) modes [6], or even in elliptical basis one obtains Ince-Gauss (IG) modes [7].

2.1 Laguerre-Gauss modes

Laguerre-Gauss modes have cylindrical symmetry along their propagation axis and are of particular interest due they carry an intrinsic Orbital Angular Momentum (OAM) due to their helicoidal phase, as a result, new applications as optical trapping [8] and optical tweezers [9] can be achieved.

The equation of the LG beam, under the paraxial assumption, in cylindrical coordinates is [7]:

$$(2.1) \quad LG_{n,l}(r, \theta, z) = \sqrt{\frac{2n!}{\pi(n+|l|)!}} \frac{1}{\omega_z} \left(\frac{\sqrt{2}r}{\omega_z} \right)^{|l|} L_n^{|l|} \left(\frac{2r^2}{\omega_z^2} \right) \exp \left[-\frac{r^2}{\omega_z^2} + i \left(l\theta + \frac{kr^2}{2R_z} - (2n+|l|+1)\phi_G \right) \right],$$

where n and l are the radial and orbital angular momentum quantum numbers, respectively, with $n \in \mathbb{Z}^{0+}$ and $l \in \mathbb{Z}$. The term $L_n^{|l|}$ corresponds to the generalized Laguerre polynomial of order n and degree $|l|$. The functions ω_z , R_z and ϕ_G are the beam waist, radius of curvature, and Gouy phase, defined as:

$$(2.2) \quad \omega_z = \omega_0 \sqrt{1 + \frac{4z^2}{k^2\omega_0^4}},$$

$$(2.3) \quad R_z = z + \frac{k^2 \omega_0^4}{4z},$$

$$(2.4) \quad \phi_G = \arctan \left[\frac{2z}{k\omega_0^2} \right],$$

where $k = 2\pi/\lambda$ is the wave number, and ω_0 is the beam waist at $z = 0$.

In the paraxial limit the angular momentum of light separates into a spin and orbital part, both of which are well defined [10], and suggests that LG modes are the eigenmodes of the angular momentum operator, \hat{L}_z , and carry OAM of $l\hbar$ per photon [6].

The radial index is so called because the intensity pattern of LG beams exhibits $n+1$ concentric rings if $l \neq 0$, and $n = 0$ rings in the case of $l = 0$. Also, the phase structure of the beam displays n concentric radial discontinuities with no smooth transitions at $z = 0$. Fig. 2.1 shows the intensity profile and phase profile of different LG modes.

The radial index is related to hyperbolic momentum [11] and generates dilations, not linear translation. As linear momentum is associated with invariance under translation, hyperbolic momentum is associated with invariance under scale transformations. Hyperbolic momentum is not a conserved quantity of paraxial photon propagation, and for the case of LG beams, hyperbolic momentum increases linearly as a function of propagation distance [11]. There also been shown that even though hyperbolic momentum is not a conserved quantity as OAM, the radial index could be in principle, used in quantum information tasks [12]. However, a caveat must be taken, since the chosen basis is waist dependent [12].

2.2 Ince-Gauss modes

Ince-Gauss modes are solutions of the paraxial wave equation in elliptical coordinate system [7], and constitute the exact and continuous transitions between Hermite-Gauss and Laguerre-Gauss. In contrast to LG modes, IG modes are described by Ince polynomials [13, 14].

The equations of the IG beams are divided into even and odd, [7]:

$$(2.5) \quad IG_{p,m}^e(\vec{r}, \varepsilon) = \frac{C\omega_0}{\omega(z)} C_p^m(i\xi, \varepsilon) C_p^m(\eta, \varepsilon) \exp \left[-\frac{r^2}{\omega_z^2} + i \left(kz + \frac{kr^2}{2R_z} - (p+1)\varphi_G \right) \right],$$

$$(2.6) \quad IG_{p,m}^o(\vec{r}, \varepsilon) = \frac{S\omega_0}{\omega(z)} S_p^m(i\xi, \varepsilon) S_p^m(\eta, \varepsilon) \exp \left[-\frac{r^2}{\omega_z^2} + i \left(kz + \frac{kr^2}{2R_z} - (p+1)\varphi_G \right) \right],$$

where C and S are the normalization constants, the superindices e and o refer to even and odd, respectively. Even and odd Ince polynomials of order p and degree m are usually denoted as $C_p^m(\eta, \varepsilon)$ and $S_p^m(\eta, \varepsilon)$, respectively, where $0 \leq m \leq p$ for even functions, and $1 \leq m \leq p$ for odd

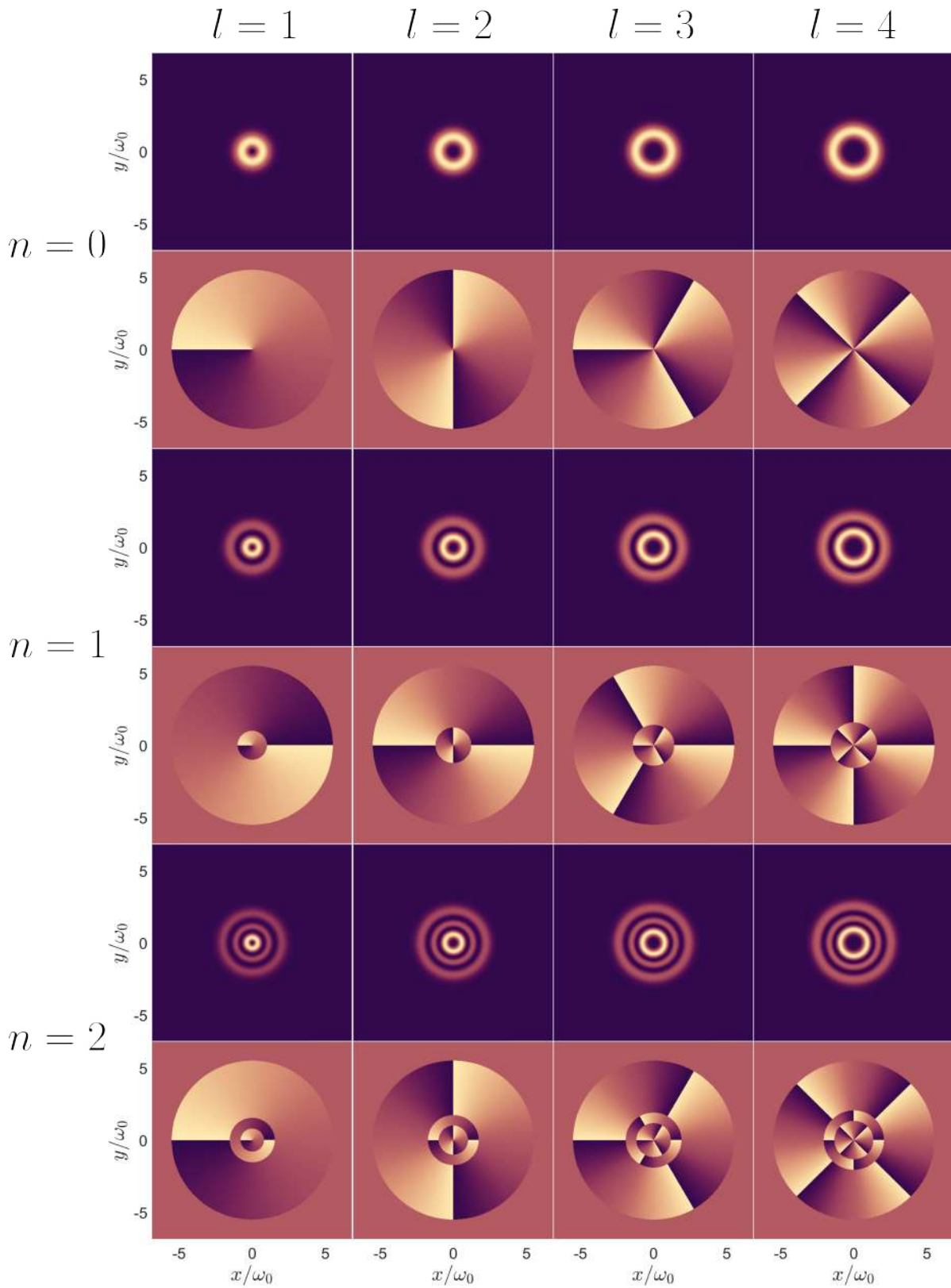


Figure 2.1: Intensity and phase profile for different LG modes, with azimuthal number $l = \{1, 2, 3, 4\}$ and radial number $n = \{0, 1, 2\}$.

functions, with $\{p, m\} \in \mathbb{Z}^+$. Also, the indices (p, m) always have the same parity, and ε is the ellipticity defined as $\varepsilon = 2f_0^2/\omega_0^2$, where f_0 is the semifocal separation at the waist plane. In comparison with LG beams, the index m represents the hyperbolic nodal lines, whereas $(p - m)/2$ is the number of elliptic nodal lines, without taking into account the interfocal nodal lines at $\xi = 0$. Fig. 2.2 a) shows the intensity and phase profile of some even IG modes for a fixed ellipticity ($\varepsilon = 2$), also Fig. 2.2 b) shows the same modes than a) with intensity and phase profile of odd IG modes. In contrast with LG beams, IG beams don't have OAM, due they don't have a helicoidal phase, therefore, when ellipticity tends to zero, the resultant mode is an LG with even or odd parity, defined as:

$$(2.7) \quad LG_{n,l}^{e,o}(r, \theta, z) = \sqrt{\frac{4n!}{(1 + \delta_{0,l})\pi(n + |l|)!}} \frac{1}{\omega_z} \begin{pmatrix} \cos(l\theta) \\ \sin(l\theta) \end{pmatrix} \left(\frac{\sqrt{2}r}{\omega_z}\right)^{|l|} L_n^{|l|}\left(\frac{2r^2}{\omega_z^2}\right) \\ \times \exp\left[-\frac{r^2}{\omega_z^2} + i\left(\frac{kr^2}{2R_z} - (2n + |l| + 1)\varphi_G\right)\right].$$

Contrary case, when ellipticity tends to infinity we obtain the HG beams defined as [7]:

$$(2.8) \quad HG_{n_x, n_y}(x, y, z) = \sqrt{\frac{1}{2^{n_x+n_y-1}\pi n_x! n_y!}} \left(\frac{1}{\omega(z)}\right) H_{n_x}\left(\frac{\sqrt{2}x}{\omega(z)}\right) H_{n_y}\left(\frac{\sqrt{2}y}{\omega(z)}\right) \\ \times \exp\left[-\frac{r^2}{\omega_z^2} + i\left(kz + \frac{kr^2}{2R_z} - (n_x + n_y + 1)\varphi_G\right)\right],$$

where H_n are the n th order Hermite polynomials. When ellipticity tends to zero, i.e. cylindrical coordinates, the modes are related as follows: $m = l$ and $p = 2n + l$. On the other hand, when ellipticity tends to infinity, the modes are related as follows: For even IG $n_x = m$ and $n_y = p - m$, whereas for odd IG $n_x = m - 1$ and $n_y = p - m + 1$. Fig. 2.3 shows the transition of HIG to an LG when ellipticity tends to zero, and the transition of HIG to an HG when ellipticity tends to infinity. Since each solution of the paraxial wave equation is an orthogonal solution, we can decompose one basis in another. We are only interested in LG and IG basis, therefore, at any plane z , the IG \leftrightarrow LG expansion is written as [15]:

$$(2.9) \quad IG_{p,m}^\sigma(\xi, \eta, \varepsilon) = \sum_{l,n} D_{l,n} LG_{n,l}^\sigma(r, \theta),$$

where $\sigma = e, o$. The coefficients $D_{n,l}$ correspond to the overlap integral between IG modes and LG modes, according to [16], the coefficients are written as:

$$(2.10) \quad \int \int_{-\infty}^{\infty} LG_{n,l}^\sigma IG_{p,m}^{\sigma'} dS = \delta_{\sigma'\sigma} \delta_{p,2n+l} (-1)^{n+l+(p+m)/2} \sqrt{(1 + \delta_{0,l})\Gamma(n + l + 1)n!} A_{l+\delta_{(o,\sigma)}/2}^\sigma(a_p^m),$$

where $A_{l+\delta_{(o,\sigma)}/2}^\sigma(a_p^m)$ is the $l + \delta_{(o,\sigma)}/2$ th Fourier coefficient of the C_p^m or S_p^m Ince polynomials. To build up a structurally stable beam, the constituent modes must have the same Gouy shift. To satisfy this condition, the summation among IG and LG must involve a finite number of modes whose indices (n, l) satisfy the relation $p = 2n + l$ for a given p .

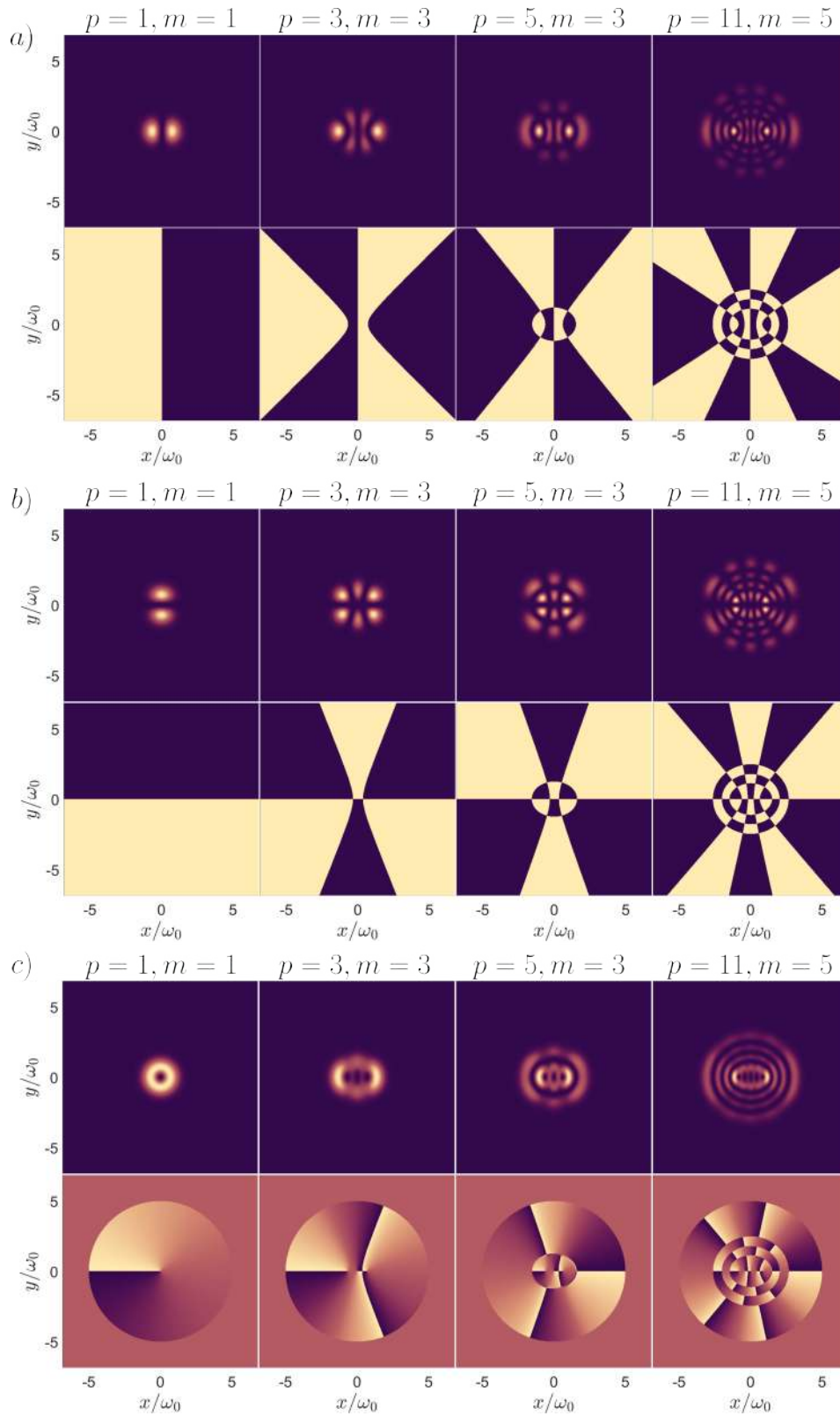


Figure 2.2: Intensity and phase profile of IG modes for a fixed ellipticity of 2. In a) Even IG modes are shown. In b) Odd IG modes are shown. In c) HIG^+ modes are shown.

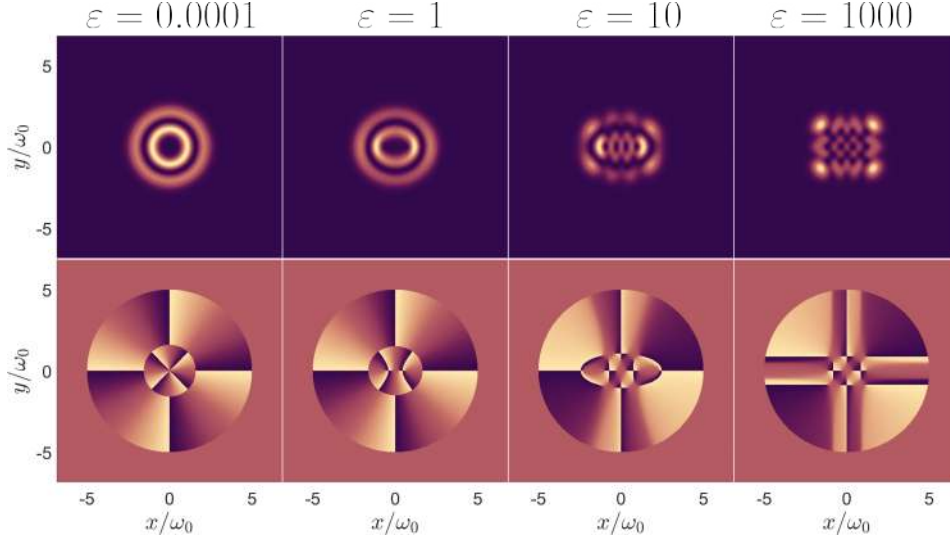


Figure 2.3: Intensity and phase profile of a $HIG_{11,6}^+$ with different values of ellipticity.

2.3 Helicoidal Ince-Gauss modes

LG beams have azimuthal angular dependence described by $\exp(\pm il\theta)$, that we can decompose in even or odd stationary phase by $\cos(l\theta)$, $\sin(l\theta)$, respectively. Similarly, we can construct Helicoidal Ince-gauss (HIG) modes of the form:

$$(2.11) \quad HIG_{p,m}^{\pm} = IG_{p,m}^e(\xi, \eta, \epsilon) \pm iIG_{p,m}^o(\xi, \eta, \epsilon),$$

but whose phase rotates elliptically, and the sign defines the rotating direction. Equation (2.11) is valid for $m > 0$, because $IG_{p,m}^o(\xi, \eta, \epsilon)$ is not defined for $m = 0$. Another interesting feature of IG photons is unlike LG photons, HIG photons have fractional OAM [17]. Fig. 2.4 shows the variation in OAM value for ellipticity for different p and m values. We can obtain this writing quantum LG modes in terms of even and odd modes:

$$(2.12) \quad |LG_{n,l}^e\rangle = \frac{1}{\sqrt{2}}(|LG_{n,l}^+\rangle + |LG_{n,l}^-\rangle),$$

$$(2.13) \quad |LG_{n,l}^o\rangle = \frac{1}{i\sqrt{2}}(|LG_{n,l}^+\rangle - |LG_{n,l}^-\rangle),$$

where, $LG_{n,l}^{\pm}$ are the quantum Laguerre-Gauss Fock states, which are eigenvectors of the OAM operator, \hat{L}_z , previously discussed in section 2.1. We can write the action of the OAM operator on equations (2.12) and (2.13) as:

$$(2.14) \quad \hat{L}_z |LG_{n,l}^e\rangle = i\hbar l |LG_{n,l}^o\rangle,$$

$$(2.15) \quad \hat{L}_z |LG_{n,l}^o\rangle = -i\hbar l |LG_{n,l}^e\rangle.$$

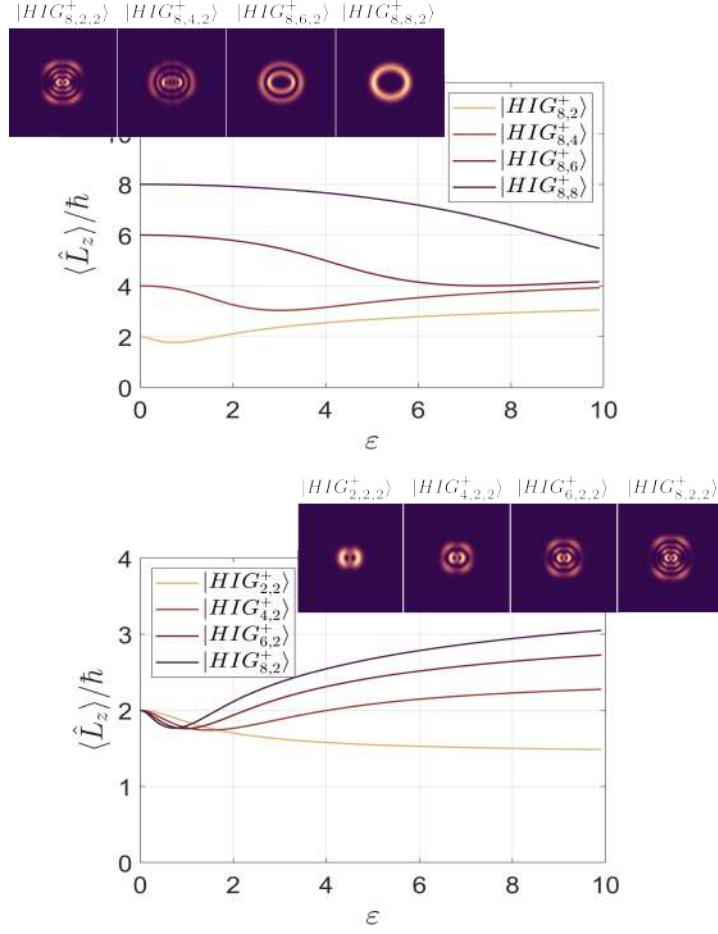


Figure 2.4: The upper figure shows different HIG with a fixed order $p = 8$ and different degrees $m = \{2, 4, 6, 8\}$. The intensity profiles have an ellipticity of $\epsilon = 2$. We can observe that when ellipticity tends to zero, the OAM value converges to the corresponding m value, i.e., the OAM of the LG mode, $m = |l|$. In the bottom figure different HIG with a fixed degree $m = 2$ and different orders $p = \{2, 4, 6, 8\}$. The intensity profiles have an ellipticity of $\epsilon = 2$. In the same way as the left figure, OAM values converge to $m = |l|$ when ellipticity tends to zero. The nomenclature of $|HIG_{p,m,\epsilon}^+\rangle$ corresponds to positive Helicoidal Ince-Gauss with subscripts order, degree, and ellipticity, respectively.

Doing the same procedure for HIG photons, using equation (2.9) on equation 2.11 we obtain:

$$(2.16) \quad |HIG_{p,m}^\pm\rangle = \frac{1}{\sqrt{2}} \left(\sum_{n,l} D_{n,l}^e |LG_{n,l}^e\rangle \pm i \sum_{n',l'} D_{n',l'}^o |LG_{n',l'}^o\rangle \right).$$

It is then straightforward to calculate the expectation value of the quantum OAM as a function of these expansion coefficients [17],

$$(2.17) \quad \langle \hat{L}_z \rangle = \pm \sum_{n,l} \hbar l D_{n,l}^e D_{n,l}^o.$$

THEORY OF TURBULENCE

In free-space optical communication (FSOC), turbulence has been an object of study due to the losses that it generates [19], also, OAM based FSOC has increased interest because OAM can be used as data carriers for mode-division multiplexing and potentially improve the communication system capacity [20, 21].

3.1 Statistical description of atmospheric turbulence

Refractive index fluctuations in the atmosphere are a direct consequence of the temperature fluctuations resulting from the turbulent motion of the air due to winds and convection. Earth's atmosphere can be considered a viscous fluid with two states of motion: laminar and turbulent. In turbulent flow, air of different temperatures mixes, so the velocity field is no longer uniform, and it acquires randomly distributed pockets of air, called turbulent eddies [19].

Kolmogorov developed a statistical theory of turbulence [22], he suggested that the kinetic energy of larger eddies is transmitted onto smaller eddies. This is known as an energy cascade theory. The average size of the largest eddies, L_0 , is known as the outer scale and the average size of the smallest eddies, l_0 , is known as the inner scale. The range between the outer and inner scales is called the inertial sub-range.

In his study, Kolmogorov obtained constant increases in the refractive index, by assuming that the eddies within the inertial sub-range are statistically homogeneous and isotropic within small regions of space. This allowed him to determine that the average speed of turbulent eddies, v , must be proportional to the cubic root of the scale size of eddies, demonstrating that the structure function of the wind velocity in the inertial sub-range satisfies:

$$(3.1) \quad D_v = \langle [v(\vec{x}_1) - v(\vec{x}_2)]^2 \rangle = C_v^2 r^{2/3}, \quad l_0 \leq r \leq L_0,$$

where $v(\vec{x})$ is the turbulent component of velocity at the point \vec{x} , $r = |\vec{x}_1 - \vec{x}_2|$ is the distance between to observation points and C_v^2 is the velocity structure constant (with units of $\text{m}^{4/3}\text{s}^{-2}$). When $r \ll l_0$, which is small scale size, the structure function satisfies the relation:

$$(3.2) \quad D_v = C_v^2 l_0^{-4/3} r^2, \quad 0 \leq r \leq l_0.$$

In the case of a larger size scale, there is no general description of the structure function, this is because in that limit, the fluctuations are anisotropic [19].

Kolmogorov's model was extended by Obukhov [18] to obtain a model of statistical description of refractive index fluctuations, obtaining the structure function for the refractive index of the form:

$$(3.3) \quad D_n(r) = \langle [n(\vec{x}_1) - n(\vec{x}_2)]^2 \rangle = \begin{cases} C_n^2 l_0^{-4/3} r^2, & 0 \leq r \leq l_0, \\ C_n^2 r^{2/3}, & l_0 \leq r \leq L_0, \end{cases}$$

where C_n^2 is the index of refraction structure constant (with units of $\text{m}^{-2/3}$), it measures the local turbulence strength. The value C_n^2 is altitude dependent, generally for the near ground have a range of $10^{-17} \text{m}^{-2/3}$ to $10^{-13} \text{m}^{-2/3}$, for weak and strong turbulence, respectively [19]. When light propagates in a horizontal path, i.e. constant altitude, it is reasonable to consider C_n^2 as a constant. This assumption is no longer valid for vertical propagation.

3.2 Power spectra of refractive index fluctuations

The effect of the turbulence on an optical wave generates random phase modulations that are introduced along the propagation path, mathematically, it can be expressed as:

$$(3.4) \quad \theta(\vec{X}) = k_0 \int_0^{\Delta z} \delta n(\vec{x}) dz,$$

where Δz represents the propagation distance, $\vec{x} = x\hat{i} + y\hat{j} + z\hat{k}$, and $\vec{X} = x\hat{i} + y\hat{j}$.

From equation (3.4) we can obtain interference between two beams, which gives the difference in phase, to obtain the structure function given by:

$$(3.5) \quad \begin{aligned} D_\theta(\vec{X}_1 - \vec{X}_2) &= \langle [\theta(\vec{X}_1) - \theta(\vec{X}_2)]^2 \rangle \\ &= 2[B_\theta(0) - B_\theta(\vec{X}_1 - \vec{X}_2)], \end{aligned}$$

where B_θ is the autocorrelation function, and it is related to the structure function as:

$$(3.6) \quad B_\theta(\vec{X}_1 - \vec{X}_2) = \langle \theta(\vec{X}_1)\theta(\vec{X}_2) \rangle,$$

It is important to observe that, as a consequence of the statistical properties being homogeneous across the phase functions, the autocorrelation function of the phase only depends on the relative coordinates. Moreover, given the isotropic nature of the phase functions, the autocorrelation

function of the phase effectively relies only on the magnitude of the relative coordinates. In Equation (3.4), the definition of the phase disregards an overall constant phase associated with the average refractive index, which is canceled out during interference and therefore does not contribute to the correlation function. As a result, the phase autocorrelation function can be expressed as follows:

$$(3.7) \quad B_\theta(\vec{X}_1 - \vec{X}_2) = k_0^2 \int_0^{\Delta z_1} \int_0^{\Delta z_2} \langle \delta n(\vec{x}_1) \delta n(\vec{x}_2) \rangle dz_1 dz_2,$$

which gives a direct relation between the refractive autocorrelation function and the phase autocorrelation function.

The refractive index structure function given in equation (3.3) is related to the refractive index autocorrelation function by [19]:

$$(3.8) \quad B_n(r) = \langle \delta n(\vec{x}_1) \delta n(\vec{x}_2) \rangle = B_n(0) - \frac{1}{2} D_n(r).$$

Using the Wiener-Khinchin theorem, which tells that exist a Fourier relationship between the autocorrelation function and the power spectral density of a statistical process [19, 23],

$$(3.9) \quad B_n(\vec{X}) = \frac{1}{(2\pi)^3} \int \int \int_{-\infty}^{\infty} \exp[i\vec{k} \cdot \vec{x}] \Phi_n(\vec{k}) d^3 \vec{k},$$

$$(3.10) \quad \Phi_n(\vec{k}) = \int \int \int \exp[i\vec{k} \cdot \vec{x}] B_n(\vec{x}) d^3 \vec{x}.$$

For a statistically homogeneous and isotropic atmosphere, expression simplifies to [19]:

$$(3.11) \quad \begin{aligned} B_n(r) &= \int_0^\infty k^2 \Phi_n(k) dk \int_0^\pi \sin \theta d\theta \int_0^{2\pi} \exp[ikr \cos \varphi] d\varphi \\ &= 4\pi \int_0^\infty k^2 \Phi_n(k) \left(\frac{\sin(kr)}{kr} \right). \end{aligned}$$

Combining equations (3.8) and (3.11) we obtain:

$$(3.12) \quad D_n(r) = 8\pi \int_0^\infty k^2 \Phi_n(k) \left(1 - \frac{\sin(kr)}{kr} \right) dk.$$

In order to calculate the structure function we need to invert the integral of equation (3.12), i.e., obtain the corresponding power spectrum [24]. To invert the equation we use that:

$$(3.13) \quad \frac{\partial}{\partial d} r^2 \frac{\partial}{\partial r} D_n(r) = 8\pi r \int_0^\infty k^3 \sin kr \Phi_n(k) dk,$$

solving the sine inverse transform we obtain:

$$(3.14) \quad \Phi_n(k) = \frac{1}{4\pi^2 k^2} \int_0^\infty \left(\frac{\sin(kr)}{kr} \right) \frac{\partial}{\partial r} \left(r^2 \frac{\partial}{\partial r} D_n(r) \right) dr.$$

Using $D_n(r) = C_n^2 r^{2/3}$, we obtain:

$$(3.15) \quad \Phi_n(k) = \frac{5}{18\pi^2} \Gamma\left(\frac{2}{3}\right) \sin\left(\frac{\pi}{3}\right) C_n^2 k^{-11/3} \approx 0.033 C_n^2 k^{-11/3}.$$

This is known as the Kolmogorov spectrum and it is only valid in the inertial sub-range $2\pi/L_0 \ll k \ll 2\pi/l_0$, consequently, it doesn't take the effects of the inner and outer scales into account.

There are other spectrum models which take into account the inner and outer scales. These include the von Karman Spectrum [19, 25] which considers the effect of the outer scale and is given by:

$$(3.16) \quad \Phi_n^{vK}(k) = 0.033C_n^2(k^2 + k_0^2)^{-11/6}, \quad k_0 = \frac{2\pi}{L_0}.$$

The Tatarski spectrum considers the effect of the inner scale, and it's given by [26]:

$$(3.17) \quad \Phi_n^T(k) = 0.033C_n^2 k^{-11/3} \exp\left(-\frac{k^2}{k_m^2}\right), \quad k_m = \frac{5.92}{l_0},$$

and the von Karman Tatarski [19] consider both, the inner and outer scale:

$$(3.18) \quad \Phi_n^{vKT}(k) = 0.033C_n^2(k^2 + k_0^2)^{-11/6} \exp\left(-\frac{k^2}{k_m^2}\right).$$

It is important to note that each spectrum has a different inertial sub-range. Because these models are theoretical, it has been impossible to establish which is the most suitable for describing light propagation through the turbulent atmosphere. The way to establish which model is more appropriate is directly from an experimental test. [27].

3.3 Amplitude variations

Since atmospheric turbulence affects the amplitude of the propagating wave, it could be described according to the Rytov method for the solution of Maxwell equations [28]. In the Rytov method, the optical field is written as:

$$(3.19) \quad U(\vec{r}) = U_0(\vec{r}) \exp[\psi(\vec{r})],$$

where $U_0(\vec{r})$ is the vacuum solution, and $\psi(\vec{r})$ is the complex phase perturbation. It is useful to isolate amplitude and phase quantities by writing:

$$(3.20) \quad \psi = \chi + i\phi,$$

where χ is the log-amplitude perturbation, and ϕ is the phase perturbation. The Rytov method can be used with a given power spectrum model to analytically compute moments of the field for simple source fields like Gaussian beams, spherical waves, and plane waves [19, 29–31]. The log amplitude (irradiance) statistics are also important to describe the strength of scintillations. The log amplitude is defined as:

$$(3.21) \quad \sigma_\chi^2(\vec{r}) = \langle \chi^2(\vec{r}) \rangle - \langle \chi(\vec{r}) \rangle^2,$$

is a common measure of scintillation. For a plane-wave source, the log amplitude variance is given by [31]:

$$(3.22) \quad \sigma_\chi^2 = 0.563k^{7/6} \Delta z^{5/6} \int_0^{\Delta z} C_n^2(z) \left(1 - \frac{z}{\Delta z}\right)^{5/6} dz.$$

Weak fluctuations are associated with $\sigma_\chi^2 < 0.25$, and strong fluctuations with $\sigma_\chi^2 \gg 0.25$. Another quantity to measure the scintillation is Rytov variance, defined for a plane wave as:

$$(3.23) \quad \sigma_R^2 = 1.23C_n^2(\Delta z)^{11/6} k^{7/6},$$

in this case when $\sigma_R^2 < 0.3$ the fluctuations are considered to be weak, when $\sigma_R^2 \sim 1$ the fluctuations are considered to be moderated, and when $\sigma_R^2 \gg 1$ the fluctuations are considered to be strong. It is important to recall that log-amplitude variance and Rytov variance are related as $4\sigma_\chi^2 = \sigma_R^2$.

Another important parameter is the coherence radius [19], for a plane wave in Kolmogorov turbulence is defined as:

$$(3.24) \quad \rho_0 = -1.46k^2 |\Delta \vec{r}|^{5/3} \int_0^{\Delta z} C_n^2(z) dz.$$

The atmospheric coherence diameter, also called Fried parameter, [32], r_0 , is a more commonly used parameter, and it is defined as $r_0 = 2.1\rho_0$.

With all previous definitions, it is useful to write the wave structure function with Kolmogorov turbulence as [19]:

$$(3.25) \quad D^K(|\Delta \vec{r}|) = 6.88 \left(\frac{r}{r_0}\right)^{5/3}.$$

It is important to recall that in this case, due to the inertial sub-range, the inner and outer scales are assumed to be $l_0 = 0$ and $L_0 = \infty$.

Practically, there is another relationship between the phase power spectrum and the refractive index power spectrum that makes it easier to calculate the phase power spectrum and is:

$$(3.26) \quad \Phi_\phi(k) = 2\pi^2 k^2 \Delta z \Phi_n(k),$$

Then, it is straightforward to show that the phase power spectrum for the Kolmogorov, von Kármán, and von Kármán Tatarski are:

$$(3.27) \quad \Phi_\phi(k) 0.49r_0^{-5/3} k^{-11/3},$$

$$(3.28) \quad \Phi_\phi^{vK} = 0.49r_0^{-5/3} (k^2 + k_0^2)^{-11/6}$$

and

$$(3.29) \quad \Phi_\phi^{vKT} = 0.49r_0^{-5/3} (k^2 + k_0^2)^{-11/6} \exp\left(-\frac{k^2}{k_m^2}\right),$$

respectively. All this analysis is only valid in the weak turbulence regime, and it will be useful in Chapter 7.

SPONTANEOUS PARAMETRIC DOWN CONVERSION THEORY

The phenomena of the Spontaneous Parametric Down Conversion (SPDC) was predicted in 1960 [33], and demonstrated in 1970 [34]. In this process, a pump field interacts with a medium with a second-order nonlinearity, as a result, a pair of lower-frequency photons are created, these photons could be entangled in energy, momentum [35] and most recently have been demonstrated entangled in orbital angular momentum [36]. Quantum entanglement has multiple applications such as imaging [37], spectroscopy [38], optical coherence tomography [39] and quantum sensing [40].

4.1 Theoretical derivation of SPDC: classical regime

Assuming no external charges, no currents, and a non-magnetic medium, also considering the standards relations $\vec{D} = \epsilon_0 \vec{E} + \vec{P}$ for the displacement, where \vec{P} is the polarisation vector of the medium, and $B = \mu_0 \vec{H}$ for the magnetic field, it is possible to obtain the wave equation (4.1) [41]:

$$(4.1) \quad \nabla^2 \vec{E} - \frac{1}{c^2} \frac{\partial^2 \vec{E}}{\partial t^2} = \frac{1}{\epsilon_0 c^2} \frac{\partial^2 \vec{P}}{\partial t^2},$$

with the polarisation $\vec{P} = \vec{P}^L + \vec{P}^{NL}$ containing linear and nonlinear terms. Considering that SPDC is a three-wave interaction we only consider the first nonlinear term, thus polarisation is given by:

$$(4.2) \quad P_i^{NL} = \epsilon_0 \sum_j \sum_k \chi_{ijk}^{(2)} \cdot E_j E_k,$$

where $\chi_{ijk}^{(2)}$ is the second order nonlinear susceptibility of the medium. Under the assumption of no-pump depletion, it is possible to solve equation (4.1) by a solution of the form [41]:

$$(4.3) \quad E_3(z, t) = A_3 e^{(k_3 z - \omega t)} + c.c.,$$

where $k_3 = n_3\omega_3/c$. To obtain the polarisation solution we substitute equation (4.3) in equation (4.1), obtaining:

$$(4.4) \quad P_3(z, t) = 4\epsilon_0 d_{\text{eff}} E_1 E_2 e^{(k_3 z - \omega t)} + c.c.$$

E_1 and E_2 are the amplitudes of the incident electromagnetic fields. d_{eff} is the effective susceptibility tensor which depends on both the geometrical factors and the type of material. One can find the following equation from equations (4.1, 4.3, 4.4):

$$(4.5) \quad \frac{d^2 A_3}{dz^2} + 2ik_3 \frac{dA_3}{dz} = -\frac{4d_{\text{eff}}\omega_3}{c^2} A_1 A_2 e^{i(k_1 + k_2 - k_3)z}.$$

The last equation can be reduced by assuming the slowly varying amplitude approximation, therefore, the first term is neglected. To find a solution to this equation under the non-depleted pump approximation it is necessary to integrate from 0 to the length of the crystal L , and considering that $I_i = 2n_i\epsilon_0 c |A_i|^2$ is the optical intensity of the i beam:

$$(4.6) \quad I_3 = \frac{8d_{\text{eff}}\omega_3^2 I_1 I_2}{n_1 n_2 n_3 \epsilon_0 c^3} L^2 \left(\frac{\sin \Delta k L / 2}{\Delta k L / 2} \right)^2,$$

with $\Delta k = k_1 + k_2 - k_3$ being the parameter called phase-matching, and ideally to have a quadratic increase $\Delta k \sim 0$. This phase-matching condition is crucial for an efficient nonlinear effect and it means a momentum conservation process. To satisfy the phase-matching condition it is necessary to fulfill the relations $k_1 + k_2 = k_3$ and equivalently $n_1\omega_1/c + n_2\omega_2/c = n_3\omega_3/c$ which implies energy conservation. These conditions are impossible to be satisfied with most materials as $n_1(\omega_1) < n_2(\omega_2) < n_3(\omega_3)$ i.e. normal dispersion. Only birefringent crystals which possess two or three (uniaxial or biaxial) refractive indices along different symmetry axes can satisfy phase-matching conditions.

Solving equation (4.5) using Manley-Rowe relations and supposing that $\Delta k = 0$ leads a solutions of the form:

$$(4.7) \quad A_1(z) = A_1(0) \cosh \left(\frac{\chi_{\text{eff}}^{(2)} |A_3|}{c} \sqrt{\frac{\omega_2 \omega_1}{n_2 n_1}} z \right),$$

$$(4.8) \quad A_2(z) = i \sqrt{\frac{\omega_2 \omega_1}{n_2 n_1}} \frac{A_3}{|A_3|} A_1^*(0) \sinh \left(\frac{\chi_{\text{eff}}^{(2)} |A_3|}{c} \sqrt{\frac{\omega_2 \omega_1}{n_2 n_1}} z \right).$$

From these results, we can see that if there is no initial incident field at frequency ω_1 , then the signal and idler beams would not exist and SPDC would not be possible.

4.2 Theoretical derivation of SPDC: quantum regime

The general principle is to start with Maxwell equations and solve this equation using the spatial Fourier expansion of the electromagnetic fields. Also, considering the Coulomb gauge $\nabla \cdot \vec{A}(\vec{r}) = 0$,

it is possible to obtain [42]:

$$(4.9) \quad \vec{A}(\vec{r}) = \vec{A}^{(+)}(\vec{r}) + \vec{A}^{(-)}(\vec{r}) = \sum_l \frac{\varepsilon_l}{\omega_l} \left(e^{i\vec{k}_l \cdot \vec{r}} \hat{a}_l + e^{-i\vec{k}_l \cdot \vec{r}} \hat{a}_l^\dagger \right) \vec{e}_l,$$

where \hat{a}_l and \hat{a}_l^\dagger corresponds to the annihilation photon operator and creation photon operator for the mode l , respectively, ε_l is the amplitude of the electromagnetic field, ω_l is the frequency of the field and \vec{e}_l is the vector associated with the direction of the field.

When the creation operator, \hat{a}_l^\dagger , acts on the vacuum state, $|\text{vac}\rangle$, it generates a single photon in mode l . Conversely, when the annihilation operator, \hat{a}_l , acts on a state containing a single photon, $|1\rangle$, it annihilates the photon, resulting in the vacuum state. Quantum optics explains the possibility of spontaneously generating a photon in a specific optical mode. This process allows a high-energy photon to spontaneously split into two (or occasionally more) photons of lower energies that were not present before the interaction with a non-linear medium.

Then, to describe the SPDC phenomena we can write the interaction Hamiltonian as:

$$\hat{H}_{\text{SPDC}} = i\hbar\kappa \left(\hat{a}_i \hat{a}_s \hat{a}_p^\dagger e^{i\vec{\Delta}k \cdot \vec{r} - i\Delta\omega t} + \hat{a}_i^\dagger \hat{a}_s^\dagger \hat{a}_p e^{-i\vec{\Delta}k \cdot \vec{r} + i\Delta\omega t} \right),$$

the first term corresponds to the second harmonic generation (SHG) phenomena (only if $\omega_s = \omega_i$), where a photon with energy $\hbar\omega_p = \hbar\omega_s + \hbar\omega_s$ is created from the annihilation of two photons, therefore, the relation $\Delta\omega = \omega_p - \omega_s - \omega_i = 0$ is fulfilled and energy is conserved. The second term corresponds to the SPDC phenomena, where a pump photon is annihilated, as a result, two photons with energies $\hbar\omega_s$ and $\hbar\omega_i$ are created. The term $\Delta k = k_p - k_s - k_i$ is known as phase matching and represents momentum conservation. We can observe in equation (4.2) that SPDC and SHG do exist at the same time. The indices $\{s, i, p\}$ are for signal, idler, and pump photons. Also, the κ constant is given by:

$$(4.10) \quad \kappa = \frac{2}{3} \frac{d_{\text{eff}}}{\varepsilon_0 V} \sqrt{\frac{\omega_p \omega_s \omega_i}{2\varepsilon_0 V}}.$$

If we consider an incoming pump beam with N_p number of photons on a nonlinear crystal, then, we can describe the incoming pump beam as the state $|0_s, 0_i, N_p\rangle$. Applying the Schrödinger equation in time and making a Taylor expansion of the exponential Hamiltonian to obtain the SPDC state we obtain:

$$(4.11) \quad |\psi(t)_{\text{SPDC}}\rangle \approx C_0 |0_s, 0_i, N_p\rangle + C_1 \frac{1}{i\hbar} \int_0^t \hat{H}_{\text{SPDC}}(t') dt' |0_s, 0_i, N_p\rangle + \dots,$$

where C_i are the coefficients of the Taylor expansion. Since we are looking for phase matching condition $\Delta k = 0$ and energy conservation $\Delta\omega = 0$, then integral in equation (4.11) is a Dirac function, applying the operators to the state we find:

$$(4.12) \quad |\psi(t)_{\text{SPDC}}\rangle = C_0 |0_s, 0_i, N_p\rangle + \kappa C_1 |1_s, 1_i, N_p - 1\rangle.$$

If we consider that the pump beam is strong enough then we can consider the electromagnetic field classical $\hat{a}_p \approx E_p$, as a result, the intensity of the SPDC process will be proportional to

the intensity of the incident beam. Recalling that $C_0 \gg C_1$, the SPDC is an inefficient process, therefore, the incident pump beam must be strong enough to obtain higher orders.

SPIRAL BANDWIDTH OF SPDC

As previously discussed in Chapter 4, when a pump field interacts with a nonlinear crystal, the result is the creation of a pair of photons with lower frequencies. It has been demonstrated that these two generated photons can be entangled in the spatiotemporal structure of light for both type-I [43] and type-II [44] SPDC. Also, entanglement has been demonstrated between spatial modes carrying orbital angular momentum [45], and this has been used for quantum information protocols [46, 47].

5.1 General amplitudes and structure of SPDC

We can consider the equation (4.12) at the output of the nonlinear crystal in the wave-vector domain to obtain [48]:

$$(5.1) \quad |\psi_{\text{SPDC}}\rangle = \int \int d\vec{k}_s d\vec{k}_i \Phi(\vec{k}_s, \vec{k}_i) \hat{a}_s^\dagger \hat{a}_i^\dagger |0\rangle,$$

where $\Phi(\vec{k}_s, \vec{k}_i)$ describes the mode function of the pump and the phase matching conditions, $|0\rangle$ is the multimode vacuum state and $\hat{a}_s^\dagger, \hat{a}_i$ is creation operators for the signal and idler modes with wave vectors \vec{k}_s, \vec{k}_i , respectively.

Generated photons are entangled in OAM modes, to solve equation (5.1) in a natural way, we describe the down-converted photons in Laguerre-Gauss modes, LG_p^l . Where l corresponds to the angular momentum carried by the mode, and p is the radial zero crossing. To obtain the coincidence probability of finding one signal photon in LG mode with l_s, p_s numbers and one idler photon in LG mode with l_i, p_i numbers we must calculate $P_{p_s, p_i}^{l_s, l_i} = |C_{p_s, p_i}^{l_s, l_i}|^2$, where the

coincidences amplitudes are given by the overlap integral,

$$(5.2) \quad \begin{aligned} C_{p_s, p_i}^{l_s, l_i} &= \langle \psi_s, \psi_i | \psi_{\text{SPDC}} \rangle \\ &= \int \int d^3 k_s d^3 k_i \Phi(\vec{k}_s, \vec{k}_i) [LG_{p_s}^{l_s}(\vec{k}_s)]^* [LG_{p_i}^{l_i}(\vec{k}_i)]^*. \end{aligned}$$

The pump and phase matching information are in function $\Phi(\vec{k}_s, \vec{k}_i)$, and we can express as [49]:

$$(5.3) \quad \Phi(\vec{k}_s, \vec{k}_i) = \int d^3 k_p \tilde{E}_p(\vec{k}_p) \xi(\vec{k}_p - \vec{k}_s - \vec{k}_i) \delta(\omega_p - \omega_s - \omega_i),$$

where the δ term ensures energy conservation, and ξ corresponds to phase matching condition. If we assume a monochromatic Gaussian pump with frequency $\omega_p = \omega_s + \omega_i$, and we apply the Fourier transform to the field to have the transverse component \vec{q} instead of wave vector \vec{k} we obtain:

$$(5.4) \quad \tilde{E}_p(\vec{k}_p) = \mathcal{F} \left\{ \frac{\sqrt{2}}{\pi} \frac{1}{\omega_p} \exp\left(\frac{-r^2}{\omega_p^2}\right) \right\}$$

And if we consider a crystal of finite thickness, L , in the longitudinal direction and transverse length much larger than the pump beam size, the phase matching condition is [49]:

$$(5.5) \quad \xi(\vec{k}_p - \vec{k}_s - \vec{k}_i) = \delta(q_p - q_s - q_i) \sqrt{\frac{L}{\pi k_p}} \text{sinc}\left(\frac{L \Delta k_z}{2}\right) \exp\left(\frac{-iL \Delta k_z}{2}\right),$$

where Δk_z is the phase matching condition along the z-direction. If the angle between signal and idler beams is small, then the momentum vector $\sqrt{k^2 - q^2}$ can be approximated by $k - q^2/2k$, and we can write the phase matching function as:

$$(5.6) \quad \Phi(\vec{k}_s, \vec{k}_i) = \frac{\omega_p}{\sqrt{(2\pi)}} e^{-\frac{\omega_p^2}{4} |\vec{q}_s + \vec{q}_i|^2} \sqrt{\frac{2L}{\pi^2 k_p}} \text{sinc}\left(\frac{L |\vec{q}_i - \vec{q}_s|^2}{4k_p}\right) e^{-i \frac{L |\vec{q}_i - \vec{q}_s|^2}{4k_p}}.$$

Equation (5.2) can be solved in a cylindrical coordinate system to obtain in a natural way angular momentum conservation $l_s + l_i = 0$. In the limit of a thin crystal, equation (5.2) can be solved analytically and gives [50]:

$$(5.7) \quad C_{p_i, p_s}^{l, -l} \propto K_{p_i, p_s}^{|l|} \frac{(1 - \gamma_i^2 + \gamma_s^2)^{p_i} (1 + \gamma_i^2 - \gamma_s^2)^{p_s} (-2\gamma_i \gamma_s)^{|l|}}{(1 + \gamma_i^2 + \gamma_s^2)^{p_i + p_s + |l|}} {}_2F_1 \left[-p_i, -p_s; -p_i - p_s - |l|; \frac{1 - (\gamma_i^2 + \gamma_s^2)^2}{1 - (\gamma_i^2 - \gamma_s^2)^2} \right]$$

where γ_i, γ_s are the ratios $\omega_p/\omega_i, \omega_p/\omega_s$ respectively, which are the inverse signal and idler widths normalized to the pump width. ${}_2F_1$ is the Gauss hypergeometric function, and $K_{p_i, p_s}^{|l|}$ is the combinatorial coefficient defined as [50]:

$$(5.8) \quad K_{p_i, p_s}^{|l|} = \frac{(p_i + p_s + |l|)!}{\sqrt{p_i! p_s! (p_i + |l|)! (p_s + |l|)!}}.$$

Since we are interested in collinear SPDC, we consider $\vec{q}_i = \vec{q}_s = 0$, therefore, sinc term in phase matching condition given in equation (5.6) is equal to one. Then, equation (5.2) is reduced to [50]:

$$(5.9) \quad C_{p_i, p_s}^{l, -l} \propto \int_0^{2\pi} d\phi \int_0^\infty r dr [LG_0^0(r, \phi)] [LG_{p_s}^{l_s}(r, \phi)]^* [LG_{p_i}^{l_i}(r, \phi)]^*.$$

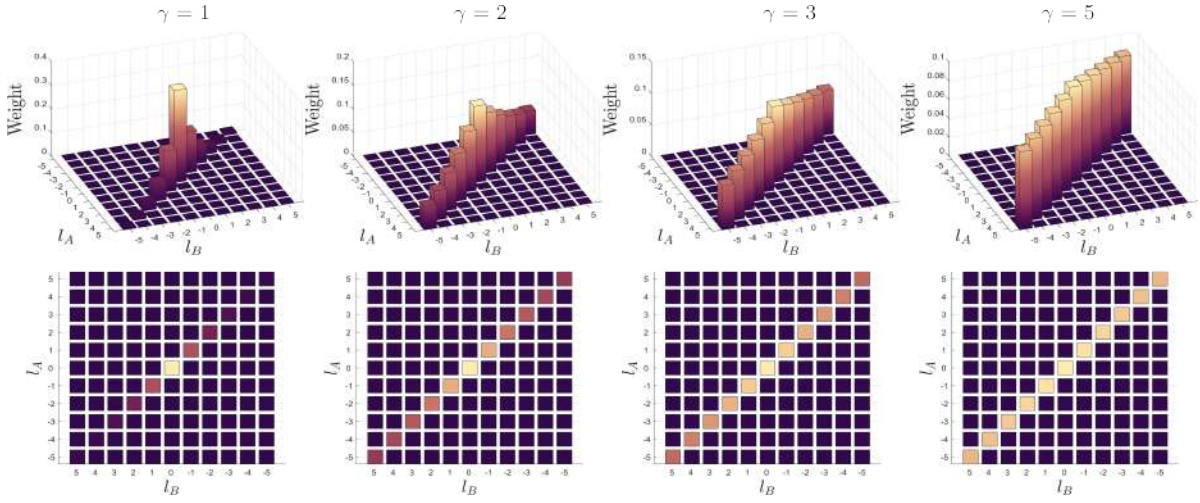


Figure 5.1: Spiral Bandwidth for different values of γ . Correlation between l values are shown for $p_s = p_i = 0$.

Generally, $\gamma_i = \gamma_s = \gamma$. Considering the case that $p_s = p_i = 0$, we can simplify the equation (5.7) to obtain a weight distribution for OAM correlation [48, 50]:

$$(5.10) \quad |C_{0,0}^{l,-l}|^2 \propto \left(\frac{2\gamma^2}{1+2\gamma^2} \right)^{2|l|}.$$

Fig. 5.1 shows the effect of the γ factor in equation (5.10). The labels A, B correspond to signal and idler photons. As γ increases, the probability of obtaining correlations for high values in OAM increases as well. This is useful for generating high OAM entanglement, but obtaining a high γ value could be challenging. Since the radial index is not conserved, the correlation in the radial index is not expected. Fig. 5.2 shows the effect of γ on p for different values of l . In all the distributions if γ increases the correlation between radial index is better. In the case of the effect of l , we have a not desirable effect, as l increases the correlation is lost. Therefore, to obtain the best correlation in radial index number, we need to implement a higher value of γ .

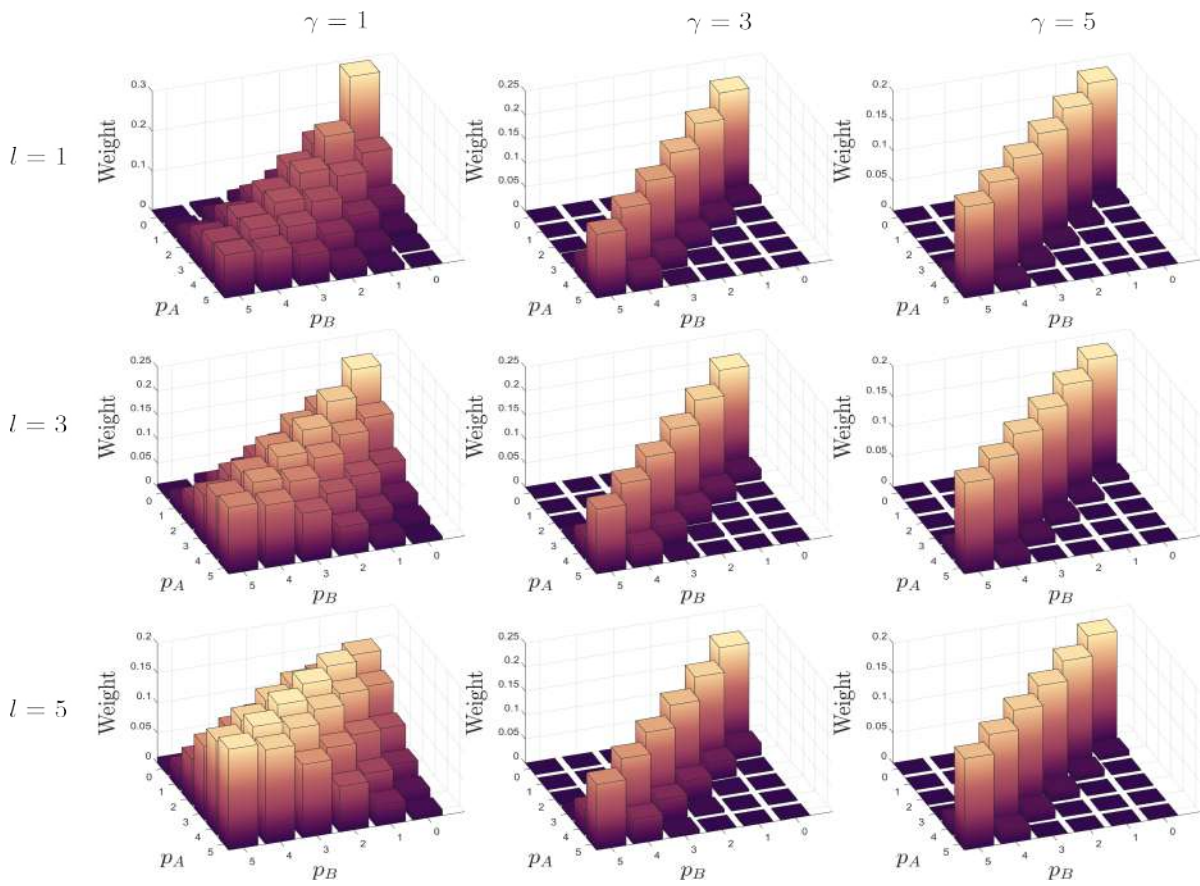


Figure 5.2: Spiral Bandwidth for different values of γ . Correlation between l values are shown, for $p_s = p_i = 0$.

ENTANGLED PHOTONS

Entanglement is considered to be the most nonclassical manifestation of quantum formalism. The entanglement was used by Einstein, Podolsky, and Rosen (EPR) in their attempt to ascribe values to physical quantities before measurement [51]. Bell formalized the EPR idea of a deterministic world in terms of the local hidden variable model. This model assumes that measurement results are determined by properties the particles carry before, and independent of, the measurement, this is known as realism, also assumes that results obtained at one location are independent of any actions performed at spacelike separation, this is known as locality [52]. Bell proved that the above assumptions impose constraints in the form of the Bell inequalities on statistical correlations in experiments involving bipartite systems. He then showed that the probabilities for the outcomes obtained when some entangled quantum state is suitably measured violate the Bell inequality. In this way, entanglement is that feature of quantum formalism that makes it impossible to simulate quantum correlations within any classical formalism [52].

6.1 Quantum Formalism

If we consider a multipartite system consisting of n subsystems, according to classical description the total state space of the system is the Cartesian product of the n subsystems. In contrast, according to quantum formalism, the total Hilbert space H is a tensor product of the subsystems spaces, mathematically, $H = \otimes_{l=1}^n H_l$. Then, a superposition principle allows us to write the total state as:

$$(6.1) \quad |\psi\rangle = \sum_{i_1, \dots, i_n} c_{i_1 \dots i_n} |i_1\rangle \otimes \dots \otimes |i_n\rangle,$$

which cannot be described as a product of states of each subsystem, mathematically, $|\psi\rangle \neq |\psi_1\rangle \otimes \dots \otimes |\psi_n\rangle$. This means that it is in general not possible to assign a single state

vector to any one of n subsystems. It expresses formally the phenomenon of entanglement, which, in contrast to classical superposition, allows us to construct an exponentially large superposition with only a linear amount of physical resources [53].

Since we are interested in bipartite states, according to the previous definition, any bipartite pure state is called separable if and only if can be written as a product of two states corresponding to the Hilbert space of subsystems:

$$(6.2) \quad |\Psi_{AB}\rangle = |\phi_A\rangle |\psi_B\rangle.$$

In contrast, a bipartite state is called entangled if and only if cannot be written as a product of two states.

Entanglement of mixed states is no longer equivalent to being nonproduct states, as in the case of pure states. Instead, one calls a mixed state of n systems entangled if it cannot be written as a convex combination of product states. A mixed bipartite state is separable if and only if it can neither be represented nor approximated by states of the following form [53]:

$$(6.3) \quad \rho_{AB} = \sum_{i=1}^k p_i \rho_A^i \otimes \rho_B^i,$$

where $\rho_{\{A,B\}}$ is the density matrix on local Hilbert space H_A, H_b , respectively.

The Bell states are the maximally entangled states because are eigenstates of the Bell operator, and they maximally violate the Bell inequality [54]. The Bell states for a bipartite system has the form:

$$(6.4) \quad \begin{aligned} |\Phi^\pm\rangle &= \frac{1}{\sqrt{2}}(|0\rangle_A |0\rangle_B \pm |1\rangle_A |1\rangle_B), \\ |\Psi^\pm\rangle &= \frac{1}{\sqrt{2}}(|0\rangle_A |1\rangle_B \pm |1\rangle_A |0\rangle_B). \end{aligned}$$

6.1.1 Concurrence

For two qubits the measure of entanglement called concurrence was introduced for pure states by Wootters [55], obtaining a closed form defined as:

$$(6.5) \quad C = \sqrt{2(1 - \text{Tr}\rho^2)},$$

where ρ is a reduced state. Another way of representing concurrence is by an antiunitary transformation [55, 56]:

$$(6.6) \quad C = \langle \psi | \theta | \psi \rangle,$$

where θ is the antiunitary transformation, also known as spin-flip, where $\theta\psi = \sigma_y \otimes \sigma_y \psi^*$, with $*$ being the complex conjugate, and σ_y the Pauli matrix [56]. The importance of equation (6.6) is that we can consider an operator:

$$(6.7) \quad w = \sqrt{\rho} \sqrt{\bar{\rho}},$$

where $\tilde{\rho} = \theta\rho\theta$. And obtain their singular values $\lambda_1, \dots, \lambda_4$ in decreasing order. Then we have [56],

$$(6.8) \quad C(\rho) = \max\{0, \lambda_1 - \lambda_2 - \lambda_3 - \lambda_4\}.$$

In fact, for any antiunitary transformation that satisfies $\Theta = \Theta^{-1}$, the concurrence is given for the generalization of Wootters' formula,

$$(6.9) \quad C_{\Theta}(\rho) = \max\left\{0, \lambda_1 - \sum_{i=2}^d \lambda_i\right\},$$

where λ_i are the eigenvalues of the operator $\sqrt{\rho}\sqrt{\Theta\rho\Theta}$ in decreasing order [57]. The values of the concurrence go from 1 to 0 when $C(\rho) = 1$ we have a maximally entangled state. In contrast, when $C(\rho) = 0$ the entanglement is lost.

To obtain the error on the concurrence, we express the density matrix in the Bloch representation [59]

$$(6.10) \quad \rho = \sum_{i,j=0}^3 B_{ij}\sigma_j \otimes \sigma_i,$$

where $B_{ij} = \text{Tr}(\rho\sigma_i \otimes \sigma_j)$ are the Bloch coefficients, σ_0 is the 2×2 identity matrix, and $\sigma_{1,2,3}$ are the Pauli matrices. We can express the operator w as:

$$(6.11) \quad w = \sum_{i,j,k,l=0}^3 B_{ij}B_{kl}\Gamma_{ijkl},$$

where $\Gamma_{ijkl=0} = (\sigma_i\sigma_y\sigma_k^*\sigma_y) \otimes (\sigma_j\sigma_y\sigma_l^*\sigma_y)$. We calculated the error on concurrence by propagating the error on the Bloch coefficients ΔB_{ij} , which was calculated as a standard deviation of the mean, assuming B_{ij} to be statistically independent. Using standard error propagation, the error on the concurrence is [59]:

$$(6.12) \quad (\Delta C)^2 = \sum_{i=1}^4 \left(\frac{\partial C}{\partial \lambda_i}\right)^2 (\Delta \lambda_i)^2 = \sum_{i=1}^4 \left(\frac{1}{2} \frac{\Delta \lambda_i}{\sqrt{\lambda_i}}\right)^2,$$

where $\Delta \lambda_i$ are the errors on the eigenvalues of the matrix w . To calculate the errors $\Delta \lambda_i$, we first found the error on the matrix w as [59]:

$$(6.13) \quad \Delta w = \sum_{klmn=0}^3 (B_{kl}\Gamma_{mnkl} + B_{kl}\Gamma_{klmn})\Delta B_{mn}.$$

Finally, by perturbation theory of non-Hermitian matrices [59], the error on the eigenvalues as:

$$(6.14) \quad \Delta \lambda_i = W_i^\dagger \Delta w V_i,$$

where W_i and V_i are the left and right eigenvectors, respectively, of w .

NUMERICAL SIMULATION

In order to study the propagation of entangled photons in OAM through atmospheric turbulence, different methods have been proposed: The Single-phase screen method [58], where analytical results can be achieved, and the Multiple-phase screen method [59]. To ensure that the numerical simulation is correct, we compare our results with analytical results shown by two different theories: The Paterson's single phase screen (SPS) theory [58], and the Smith and Raymer two-photon wave mechanics (TWM) theory [60]. Furthermore, we compare our multiple-phase screen (MPS) results with another numerical simulation that can be found in the literature [59].

7.1 Single-Phase Screen Method

The SPS method assumes that the overall effect of the turbulent medium can be represented by a single phase distortion followed by a free-space propagation.

7.1.1 The Paterson Theory

Following the work of Paterson [58], in which he used a radial basis to obtain the probabilities for the angular momentum measurements that are given by:

$$(7.1) \quad P(l) = \int_0^\infty |R(r, z)|^2 r \Theta(r, l - l_0) dr,$$

where $R(r, z)$ is the radial complex amplitude, and $\Theta(r, l - l_0)$ is the circular harmonic transform of the rotational coherence function with an initial OAM value of l_0 and it is defined as:

$$(7.2) \quad \Theta(r, \Delta l) = \frac{1}{2\pi} \int_0^{2\pi} C_\phi(r, \Delta\theta) \exp(-i l \Delta\theta \Delta l) d\Delta\theta,$$

where C_ϕ is the rotational coherence function. Equation (7.2) is a scattering equation for OAM states between azimuthal modes. Since the scattering coefficients depend only on the difference $\Delta l = l - l_0$, for a given radial profile $R(r, z)$ the resultant OAM spreading is independent of the initial eigenvalue.

The rotational coherence function is defined as [58]:

$$(7.3) \quad C_\phi(r, \Delta\theta) = \langle \exp\{i[\phi(r, \Delta\theta) - \phi(r, 0)]\} \rangle,$$

where $\phi(r, \theta)$ is the phase perturbation due turbulent phase aberration. If we consider a Gaussian random process, $\langle \exp(ix) \rangle = \exp(-\frac{1}{2} \langle |x|^2 \rangle)$, we can use the expression given in equation (7.3) to obtain:

$$(7.4) \quad C_\phi(r, \Delta\theta) = \exp \left[-\frac{1}{2} D_\phi \left(\left| 2r \sin \left(\frac{\Delta\theta}{2} \right) \right| \right) \right],$$

where $D_\phi(|\Delta x|) = \langle |\phi(x) - \phi(x + \Delta x)|^2 \rangle$ is the phase structure function. Using Kolmogorov phase structure function, equation (3.25) of Section (3.3), $D_\phi^K = 6.88(\Delta x/r_0)^{5/3}$. Thus, the rotational coherence function at radius r is:

$$(7.5) \quad C_\phi(r, \Delta\theta) = \exp \left[-6.88 \times (2)^{2/3} \left(\frac{r}{r_0} \right)^{5/3} \left| \sin \left(\frac{\Delta\theta}{2} \right) \right|^{5/3} \right].$$

7.1.2 Analytic Concurrence

Since we are interested in the biphoton state upon transmission through turbulent media, our fundamental quantity of interest is the output density operator ρ . We can consider equation (7.1) as a mapping that represents the action of an ensemble-averaged phase screen on a single photon density operator [61], mathematically:

$$(7.6) \quad \sigma_{nl, n'l'} = \sum_{n_0 l_0, n'_0 l'_0} \Lambda_{nl, n'l'}^{n_0 l_0, n'_0 l'_0} \sigma_{n_0 l_0, n'_0 l'_0}^{(0)},$$

here $\sigma^{(0)}$, σ , are the input and output single photon density matrices, respectively, and the matrix $\Lambda_{nl, n'l'}^{n_0 l_0, n'_0 l'_0}$ have the meaning: When the indices match $n = n_0$, $l = l_0$, $n' = n'_0$ and $l' = l'_0$ describes the mapping of the initially populated OAM modes onto themselves, this is known as survival amplitude, all other elements of the matrix are known as crosstalk. For a two-photon output state ρ , is related to the input state $\rho^{(0)} = |\Psi_0\rangle \langle \Psi_0|$ as:

$$(7.7) \quad \rho = (\Lambda_1 \otimes \Lambda_2) \rho^{(0)},$$

where Λ_i , $i = 1, 2$ is the linear mapping representing the phase screen seen by either photon.

We can now describe the entanglement evolution of the states through turbulence, considering the radial quantum number of the output unobserved and traced over:

$$(7.8) \quad \Lambda_{l, \pm l}^{l_0, l'_0} = \frac{\delta_{l_0 - l'_0, l \mp l'}}{2\pi} \int_0^{infy} R_{n, l_0}(r) R_{n, l'_0}^*(r) r dr \\ \times \int_0^{2\pi} \exp \left[-6.88 \times (2)^{2/3} \left(\frac{r}{r_0} \right)^{5/3} \left| \sin \left(\frac{\Delta\theta}{2} \right) \right|^{5/3} \right] \exp \left[-i\theta \frac{l \pm l - (l_0 + l'_0)}{2} \right],$$

where R_{p,l_0} is the radial part of the LG mode at $z = 0$, with quantum radial number n , and azimuthal quantum number l_0 .

Due to the crosstalk of equation (7.6), the matrix of the output state spread over an infinite-dimensional OAM basis, to deal with this, the transmitted state is post-selected [60] in the basis of the input qubit state, $\{|-l_0, -l_0\rangle, |-l_0, l_0\rangle, |l_0, -l_0\rangle, |l_0, l_0\rangle\}$. Since such post-selection entails the decay of the output state, it needs to be renormalized by its trace [62] to obtain the concurrence. To evaluate the output entanglement in the truncated Hilbert space, we make use of the inversion symmetry [63], this is:

$$(7.9) \quad \Lambda_{l,l'}^{l_0,l'_0} = \Lambda_{-l,-l'}^{-l_0,-l'_0},$$

as a consequence, there are only two elements distinct from zero:

$$(7.10) \quad a = \Lambda_{l_0,l_0}^{l_0,l'_0} = \Lambda_{-l_0,-l_0}^{-l_0,-l'_0} = \Lambda_{-l_0,l_0}^{-l_0,l'_0} = \Lambda_{l_0,-l_0}^{l_0,-l'_0},$$

$$(7.11) \quad b = \Lambda_{l_0,l_0}^{-l_0,-l'_0} = \Lambda_{-l_0,-l_0}^{l_0,l'_0}.$$

We can observe that equation (7.10) corresponds to the survival amplitude, and equation (7.11) corresponds to the crosstalk amplitude. Now, using Woottter's concurrence formula for a mixed bipartite qubit state, an analytical expression is obtained [63]:

$$(7.12) \quad C(\rho) = \max \left[0, \frac{1 - 2(b/a)}{(1 + b/a)^2} \right].$$

Fig. 7.1 shows the plots of the concurrence against scintillation strength. Here, the scintillation strength is represented by:

$$(7.13) \quad \frac{\omega_0}{r_0} = 5.4053\omega_0 \left(\frac{C_n^2 z}{\lambda^2} \right)^{5/3},$$

where:

$$(7.14) \quad r_0 = (0.423C_n^2 k^2 z)^{-3/5},$$

is the Fried parameter defined in Chapter 3, section 3.3. The quantity ω_0/r_0 depends on the propagation distance z , and refractive-index structure constant C_n^2 . It is important to recall that there are different ways to obtain the same scintillation strength, i.e., taking long propagation in weak turbulence, or a shorter propagation through moderate turbulence. This is the reason why the quantity ω_0/r_0 is a better option to plot against concurrence, instead of propagation distance or another parameter. Fig. 7.1 also suggests that, as the value of $|l|$ increases, the photon entanglement is more robust against turbulence, regardless of the radial quantum number. To analyze the effect of the radial number on the entanglement, we plot in Fig. 7.2 the concurrence against scintillation strength for different radial numbers for a fixed OAM value, regardless of the OAM value, as the radial number increases the entanglement decays faster. This phenomenon is more evident for OAM low values.

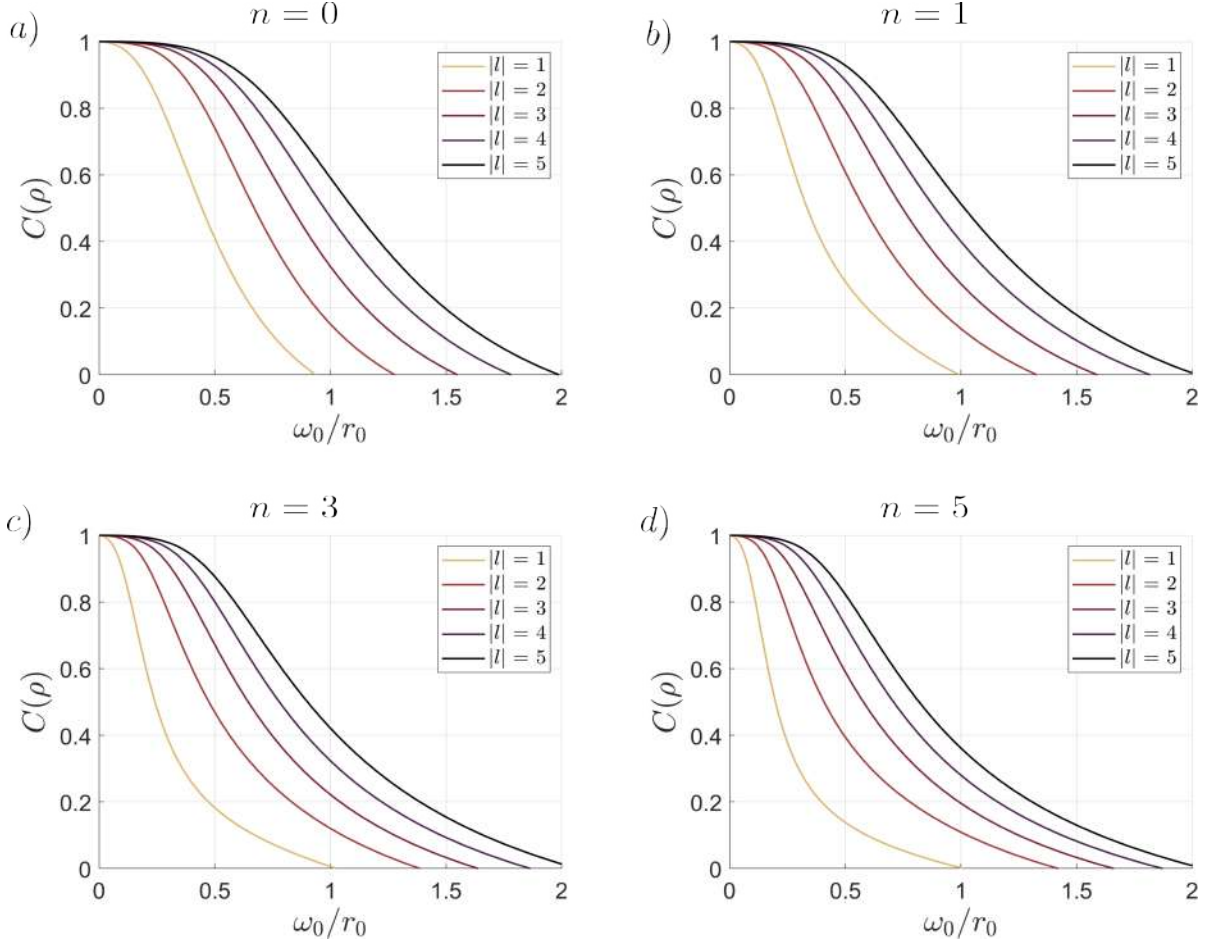


Figure 7.1: The concurrence against scintillation strength (ω_0/r_0), for different OAM values and the same radial number. In the case when two photons propagate through turbulence.
a) Quantum radial number $n = 0$. b) Quantum radial number $n = 1$. c) Quantum radial number $n = 3$. d) Quantum radial number $n = 5$.

7.1.3 Smith and Raymer theory: Two-photon wave mechanics

Another theory that we use to compare our results with is the one developed by Smith and Raymer called Two-photon wave mechanics [60]. In their work, they study the propagation of a two-photon wave function, related to the probability amplitude for finding the energies of two photons localized in two different spatial positions \vec{x}_1 and \vec{x}_2 , at the same time t . The function can be constructed from a single-photon wave function as [60]:

$$(7.15) \quad \Psi(\vec{x}_1, \vec{x}_2, t) = \sum_{l,m} C_{l,m} \psi_l^{(1)}(\vec{x}_1, t) \otimes \psi_m^{(1)}(\vec{x}_2, t),$$

where the modulus of the square coefficients $|C_{l,m}|^2$, gives the probability of the photons being in the states labeled by l and m . They assume an LG basis for photons with OAM, described by $\psi_{n,l}(r, \theta) = R_n(r) \exp(il\theta) / \sqrt{2\pi}$, where the indices have the same meaning as before. Then, the

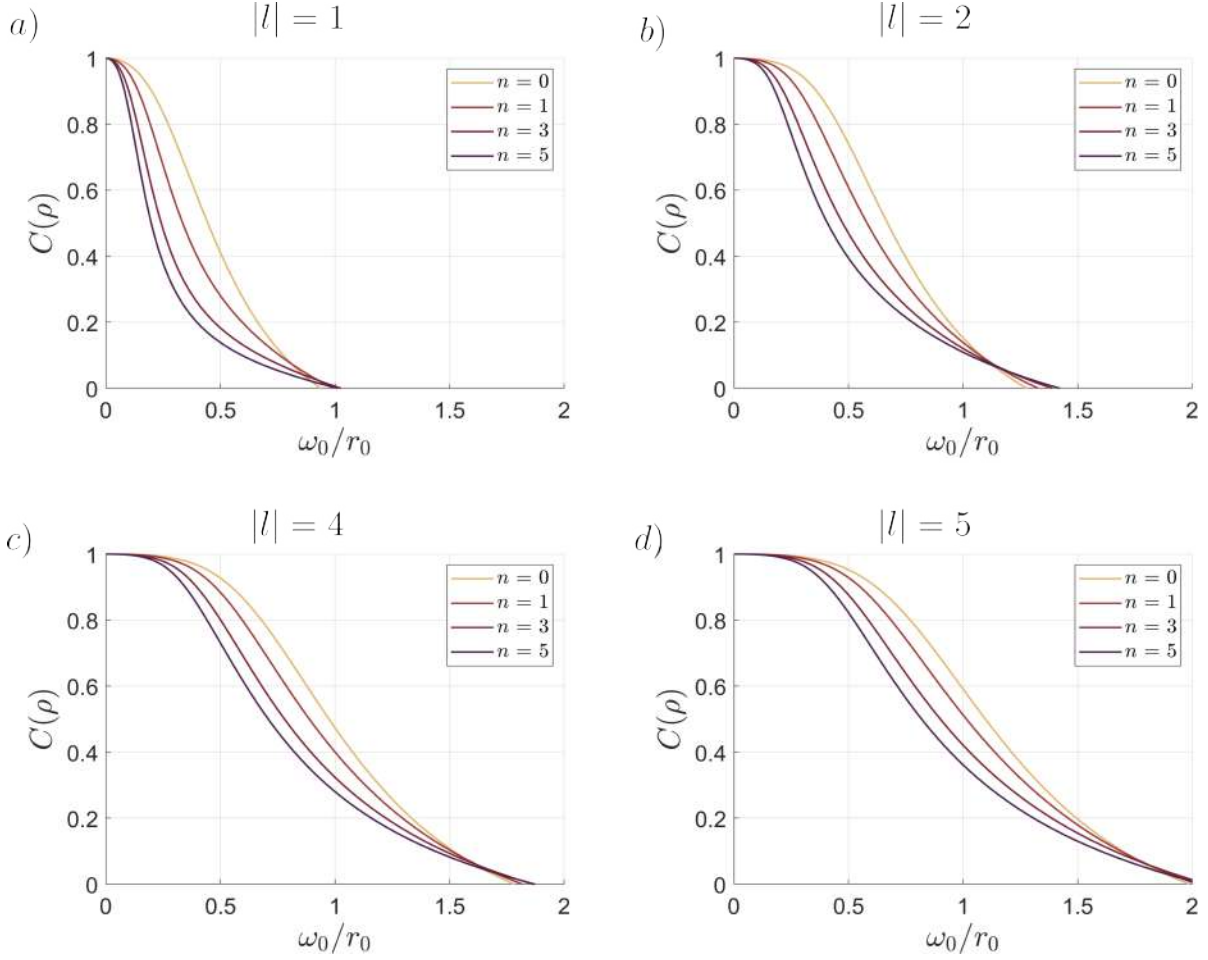


Figure 7.2: The concurrence against scintillation strength (ω_0/r_0), for different radial number and same $|l|$ value. In the case when two photons propagate through turbulence. a) OAM $|l| = 1$. b) OAM $|l| = 2$. c) OAM $|l| = 4$. d) OAM $|l| = 5$.

input pure state is:

$$(7.16) \quad \Psi_{\text{in}} = \frac{1}{\sqrt{2}}(\varphi_{A(B)}^2 + \varphi_{A(B)}^3),$$

where $\varphi_{A(B)}^2 = \psi_{n,l}^A \otimes \psi_{n,-l}^B$, and $\varphi_{A(B)}^3 = \psi_{n,-l}^A \otimes \psi_{n,l}^B$. The indices A and B corresponds to the labeled photons with the same radial quantum number n and equal OAM magnitude $|l|$.

Smith and Raymer also assume that the phase correlation function has a quadratic phase structure function dependence:

$$(7.17) \quad C_\phi(r, \Delta\theta) = \exp \left[-6.88 \times (2)^{2/3} \left(\frac{r}{r_0} \right)^2 \left| \sin \left(\frac{\Delta\theta}{2} \right) \right|^2 \right].$$

In other words, they make the approximation $5/3 \approx 2$, which enables them to obtain a closed form of the phase correlation function as:

$$(7.18) \quad C_\phi(r, \Delta\theta) = \exp \left[-2 \left(\frac{r}{r_0} \right)^2 \right] I_m \left[-2 \left(\frac{r}{r_0} \right)^2 \right],$$

where m is equal to 0 or $2l$, and I_m is the m -th order modified Bessel function.

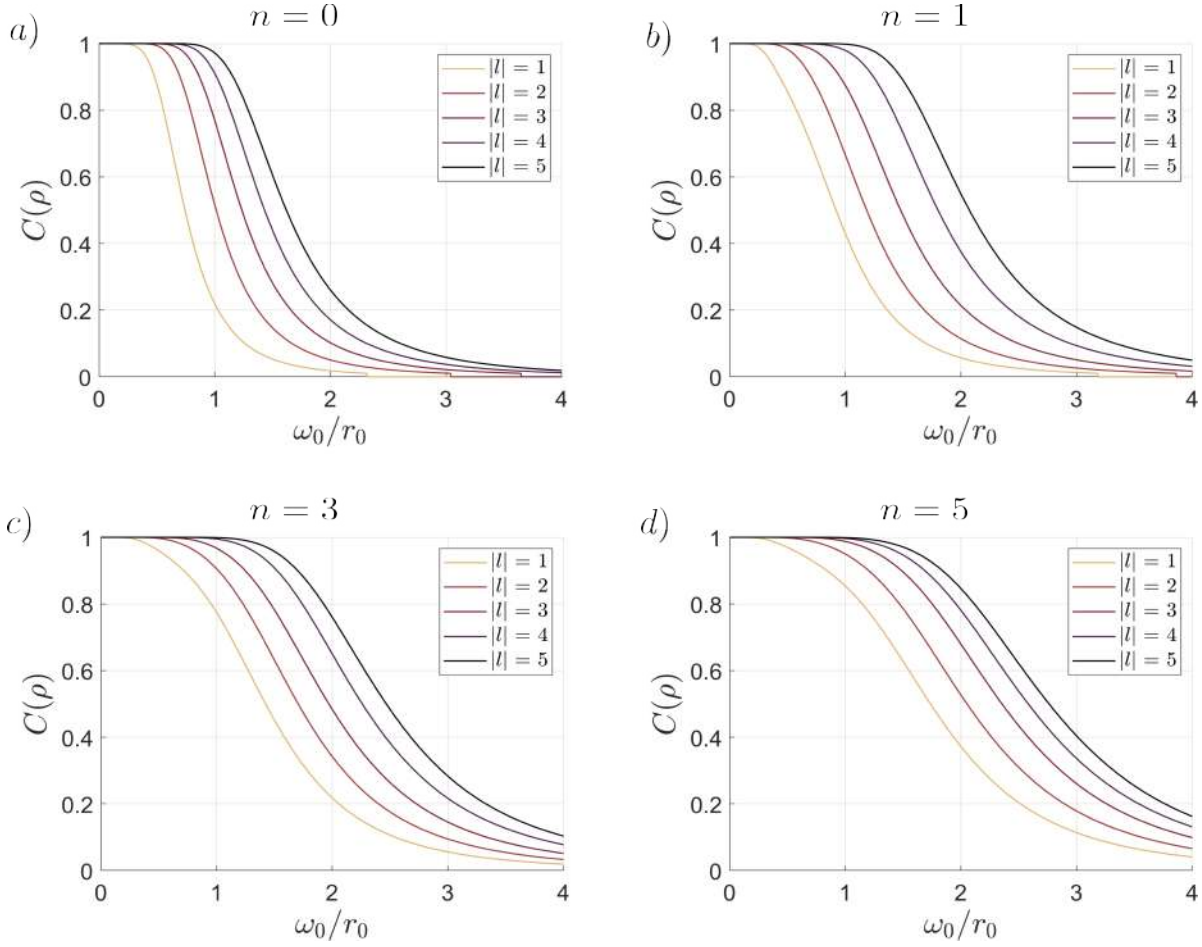


Figure 7.3: The concurrence against scintillation strength (ω_0/r_0), for different OAM values and the same radial number. In the case when two photons propagate through turbulence using TWM theory. a) Quantum radial number $n = 0$. b) Quantum radial number $n = 1$. c) Quantum radial number $n = 3$. d) Quantum radial number $n = 5$.

Unlike, Paterson and Leonhard [63] theory, the concurrence here has not an analytical expression, the concurrence must be obtained through the density matrix. To compare solutions of section 7.1.2 and TWM theory, Fig. 7.3 shows the plot of the concurrence against scintillation strength for a fixed quantum radial number n , and different OAM values, these results agree with Fig. 7.1, as $|l|$ value increases, the entanglement is more robust against turbulence, regardless of the quantum radial number. For the case of a fixed $|l|$ value and different quantum radial number n we show how Fig. 7.4 disagrees with Fig. 7.2, due as the radial quantum number increases, the entanglement is more robust.

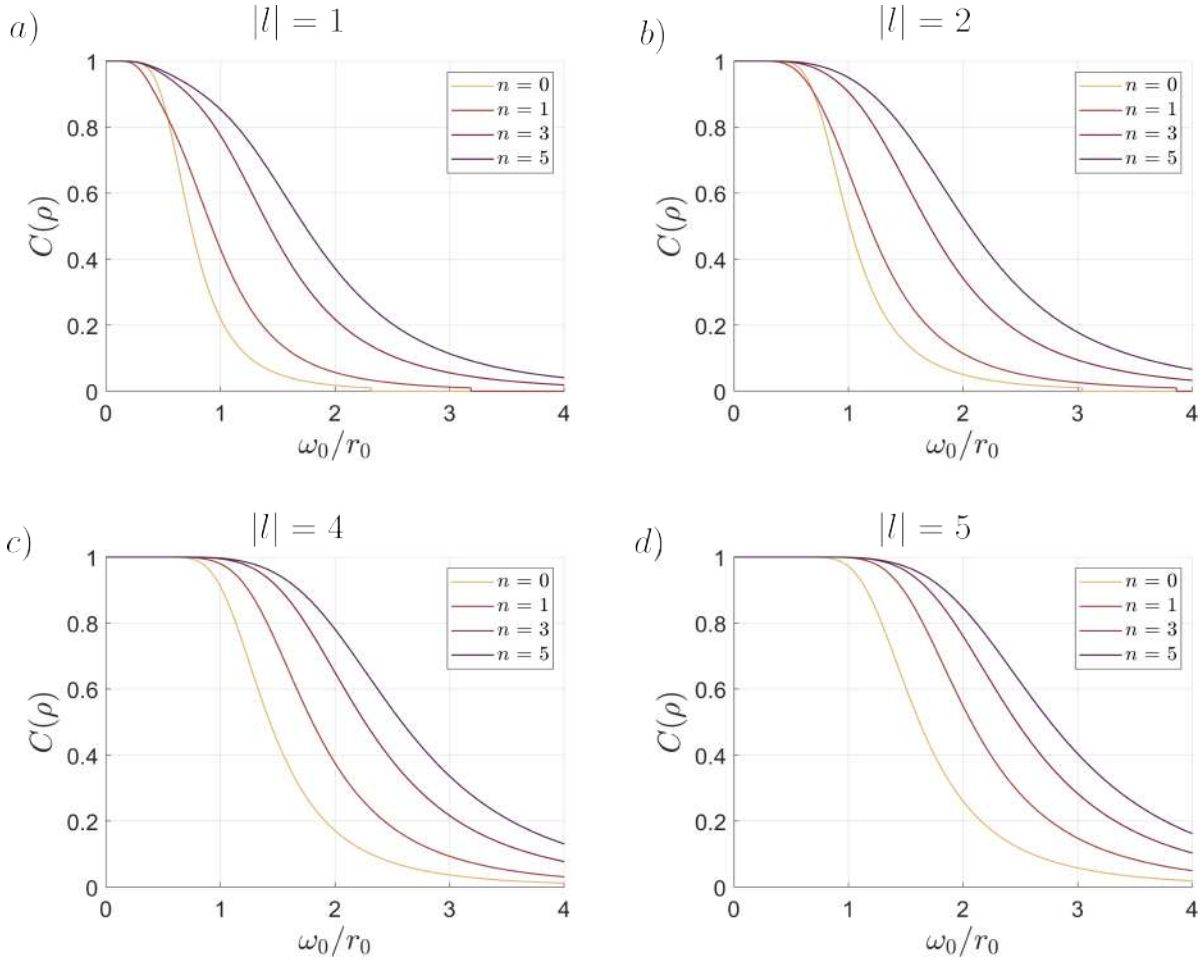


Figure 7.4: The concurrence against scintillation strength (ω_0/r_0), for different radial number and same $|l|$ value. In the case when two photons propagate through turbulence using TWM theory. a) OAM $|l| = 1$. b) OAM $|l| = 2$. c) OAM $|l| = 4$. d) OAM $|l| = 5$.

The reason why this happens is because in equation (7.12) when the crosstalk factor b , increases, the survival amplitude a decreases, until $b/a = 0.5$, in this case, concurrence is equal to zero, then, concurrence directly depends on the crosstalk integral. In the case of TWM, the coefficients obtained for each state of the density matrix are dependent on both quantities, crosstalk, and survival amplitude. Another important difference is that, for TWM theory, concurrence reaches a greater value of scintillation strength, this is because the quadratic factor on the phase structure function over-estimates the concurrence as the $|l|$ value increases, therefore, the photons have less crosstalk.

Both models presented here assume that the overall effect of the turbulence on the photons is phase distortion only, and is only valid in the weakly turbulent regime, as we previously discussed in section 3.3. To obtain a better representation of the effect of the turbulence on the OAM photon entanglement, another model known as Multiple-Phase Screen Method is presented.

7.2 Multiple-Phase Screen Method

The MPS consists in generating an arbitrary number of phase screens and performing a partial vacuum propagation between each screen. This method has been applied in many prior studies of beam propagations through turbulence [64–66]. The idea here is to corroborate that our numerical simulation agrees with previous results shown in sections 7.1.2, 7.1.3, and published results [67–69], in LG basis. Once we have corroborated our results for LG modes with zero radial index, we will extend the analysis to LG modes with non-zero radial indices, since this is an unexplored area and, although the radial mode is not conserved, it has already been used for quantum communications [70]. Once this is done, we will use HIG modes to explore the different degrees of freedom described in section 2.3.

The simulation method of beam propagation can be found in [71], but a detailed summary is presented here.

7.2.1 Geometry and Beam propagation

The geometry of the problem is described by an aperture source D_1 and an observation aperture D_2 , with a total length L , this total propagation distance is split into N equidistant steps, Δz , and each step depends on the turbulence strength across the propagation path. Once defined the geometry of the problem is, the method to propagate the beam in each partial propagation is Fresnel diffraction integral:

$$(7.19) \quad U(r_{j+1}) = \frac{1}{i\lambda\Delta z} \int_{-\infty}^{\infty} U(r_j) e^{i\frac{k}{2\Delta z}|r_{j+1}-r_j|^2} dr_j,$$

here $(j+1)$ -th term corresponds to the observation plane, in a coordinate system r_j . In equation (7.19) a scaling factor, m is added along the grid spacing, δ_j . Then, equation (7.19) is modified as:

$$(7.20) \quad U(r_{j+1}) = \frac{e^{-i\frac{k}{2\Delta z}\frac{1-m_j}{m_j}r_{j+1}^2}}{i\lambda\Delta z} \int_{-\infty}^{\infty} U(r_j) e^{i\frac{k}{2\Delta z}(1-m_j)r_j^2} e^{i\frac{km_j}{2\Delta z}\left|\frac{r_{j+1}}{m_j}-r_j\right|^2} dr_j.$$

where $m = \delta_{j+1}/\delta_j$. A detailed demonstration of equation (7.20) can be found in [75].

7.2.2 Avoiding Aliasing

To solve computationally the equation (7.20), different methods can be achieved, such as Discrete Fast Fourier Transforms (FFT), Non-Uniform Fast Fourier Transform (NUFFT) or Convolution [72–74]. Here we use FFT. According to the geometry imposed in section 7.2.1 we need to use the Nyquist criterion to place a constraint on the grid spacing such that:

$$(7.21) \quad \delta \leq \frac{1}{2f_{\max}},$$

where f_{\max} is the maximum frequency of interest. Four constraints can be obtained from equation (7.21) [75]:

$$(7.22) \quad \begin{aligned} 1. \quad & \delta_n \leq -\frac{D_2}{D_1} \delta_1 + \frac{\lambda \Delta z}{D_1}, \\ 2. \quad & N \geq \frac{D_1}{2\delta_1} + \frac{D_2}{2\delta_n} + \frac{\lambda \Delta z}{2\delta_1 \delta_n}, \\ 3. \quad & \left(1 + \frac{\Delta z}{R}\right) \delta_1 - \frac{\lambda \Delta z}{D_1} \leq \delta_n \leq \left(1 + \frac{\Delta z}{R}\right) \delta_1 + \frac{\lambda \Delta z}{D_1}, \\ 4. \quad & N \geq \frac{\lambda \Delta z}{\delta_1 \delta_n}, \end{aligned}$$

where δ_1 , δ_n corresponds to the first and final grid spacing, respectively, R is the radius of curvature, N is the number of grid points, and D_1 , D_2 are defined as follows:

$$(7.23) \quad D_1 = D'_1 + c \frac{\lambda \Delta z}{r_0},$$

$$(7.24) \quad D_2 = D'_2 + c \frac{\lambda \Delta z}{r_0},$$

here, the coefficient c is an adjustable parameter indicating the sensitivity of the model to the turbulence. Choosing $c = 2$ captures the $\sim 97\%$ of the light, and choosing $c = 4$ captures the $\sim 99\%$ of the light. D'_1 and D'_2 are the source diameter, and observation diameter, respectively.

The suggested method to solve the four constraints in equation (7.22), is to solve graphically the first three constraints and after that, choose the parameters that satisfy the four constraints. For instance, Fig. 7.5 shows the first three constraints for $\lambda = 1064$ nm, $D'_1 = D'_2 = 0.1$ m, $\Delta z = 600$ m, $R = \infty$, and $C_n^2 = 6.67 \times 10^{-15} \text{m}^{-2/3}$.

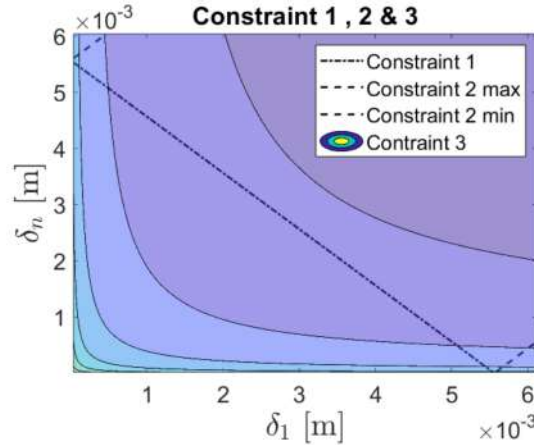


Figure 7.5: Graphical representation of the first three constraints of equation (7.22).

From Fig. 7.5 we can directly choose $\delta_1 = \delta_2 = 0.8 \times 10^{-3}$ m, which corresponds to $N = 2^9$, this value satisfies the fourth constraint. It is important to recall that these constraints are not unbreakable rules, they are only criteria to avoid aliasing.

Once, N , δ_1 , and δ_2 are chosen, the partial propagation distances and the number of partial propagations is [75]:

$$(7.25) \quad \Delta z_{\max} = \frac{\min(\delta_1, \delta_2)^2 N}{\lambda},$$

$$(7.26) \quad n_{\min} = \text{ceil}\left(\frac{\Delta z}{\Delta z_{\max}}\right) + 1$$

7.2.3 Vacuum Propagation

To verify that the beam propagation is correct, we perform a vacuum propagation, which corroborates the energy conservation and the correct mode propagation. Fig. 7.6 shows the effect of vacuum propagation on the mode. We can observe that before and after propagation the intensity of the mode has the same value, due to energy conservation. The main difference is the phase between the mode before and after propagation, we can observe that after propagation the phase has a twist, this is because of the helicoidal phase of the LG mode.

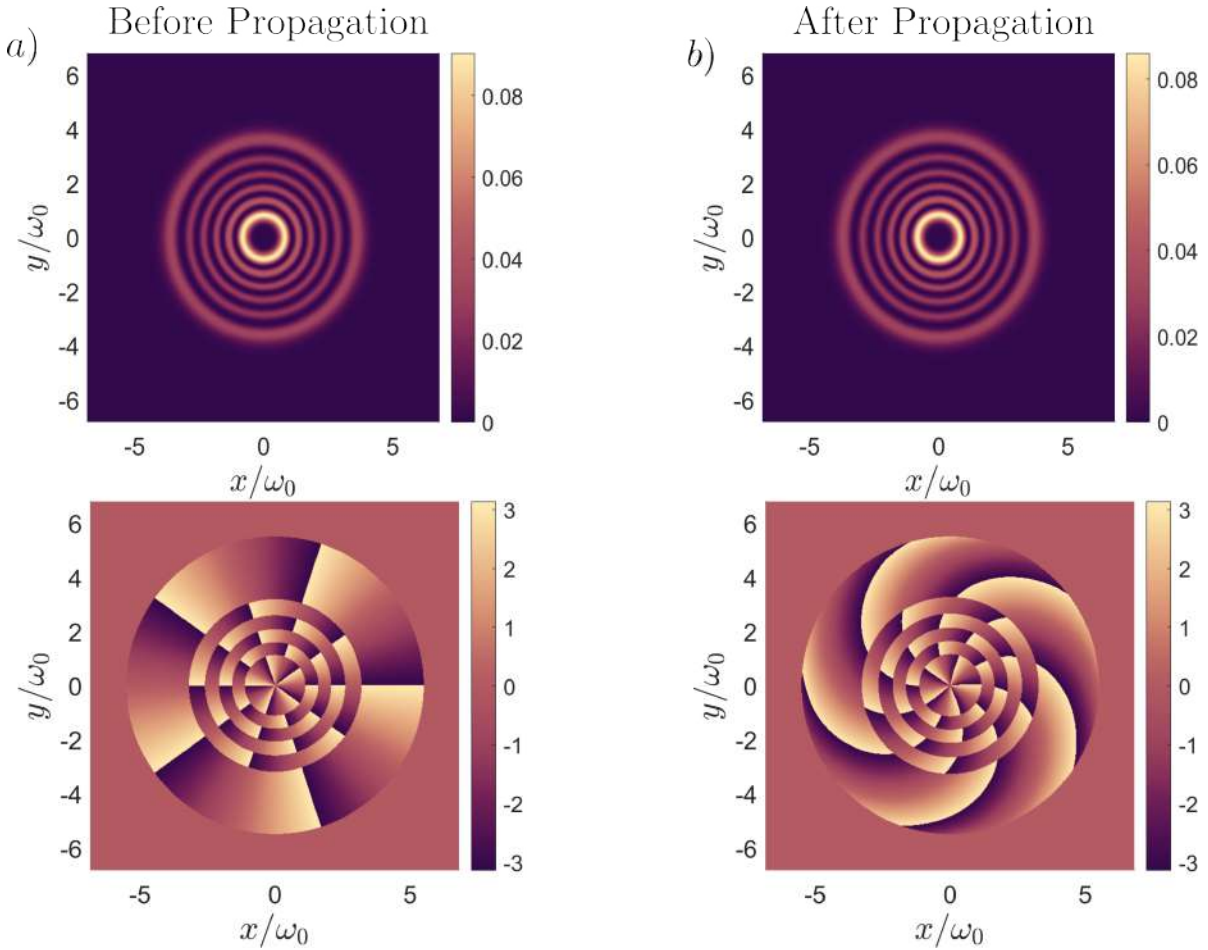


Figure 7.6: Vacuum propagation of LG mode with $l = 5$, $n = 5$. In a) the intensity and phase of the mode before propagation, in b) the intensity and phase of the mode after propagation.

7.2.4 Turbulent Phase Screen Generation

Now that we know how a beam propagates through a vacuum, it is necessary to create turbulent phase screens that are going to be imposed on the beam as it propagates.

To generate a phase screen on a finite grid, we write the optical phase as a Fourier series expansion [76]:

$$(7.27) \quad \phi(x, y) = \sum_{n=-\infty}^{\infty} \sum_{m=-\infty}^{\infty} c_{n,m} \exp[i2\pi(f_{x_n}x + f_{y_m}y)],$$

where f_{x_n} and f_{y_m} are the discrete x and y spatial frequencies, and the $c_{n,m}$ are the complex Fourier series coefficients. Using the central limit theorem to determine that the $c_{n,m}$ have a Gaussian distribution.

Since the FFT is used for computational efficiency, the frequency samples must be linearly spaced on a cartesian grid, then, equation (7.27) can be written as [76]:

$$(7.28) \quad \langle |c_{n,m}|^2 \rangle = \frac{1}{L_x L_y} \Phi_\phi(f_{x_n}, f_{y_m})$$

where $L_x = 1/\Delta f_{x_n}$ and $L_y = 1/\Delta f_{y_m}$.

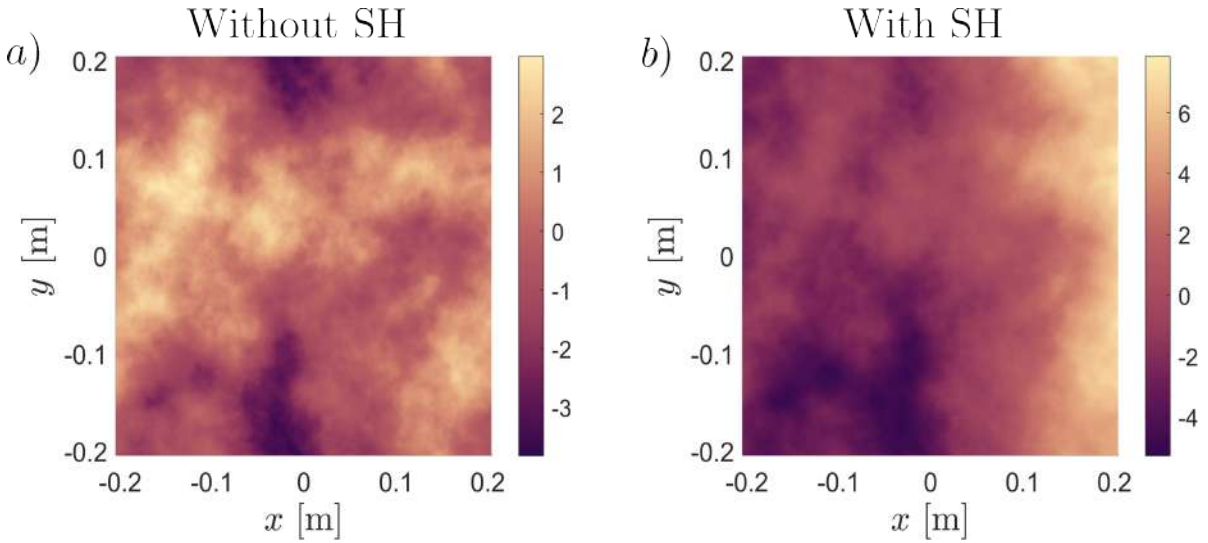


Figure 7.7: Generation of turbulent phase screens. Both a) and b) are the same phase screen, the only difference is that in a) phase screen is generated without subharmonic method, and in b) phase screen is generated with subharmonic method.

Fig. 7.7 a) shows the generation of a turbulent phase screen, unfortunately, the FFT method does not produce accurate phase screens, this is because much of the power is on the low spatial frequencies, to correct sampling a turbulent phase screen, subharmonic (SH) method is used [77]. The subharmonic method consists in creating subgrids, and uses an FT method to create a

low-frequency screen $\phi_{LF}(x, y)$, which consists of a sum of different N_p screens,

$$(7.29) \quad \phi_{LF}(x, y) = \sum_{p=1}^{N_p} \sum_{n=-1}^1 \sum_{m=-1}^1 c_{n,m} \exp[i2\pi(f_{x_n}x + f_{y_m}y)],$$

where the value of p corresponds to a different screen. The frequency grid spacing for each value of p is $\Delta f_p = 1/(3^p L)$. Fig. 7.7 b) shows a phase screen with the subharmonic method, in contrast with Fig. 7.7 a) the phase screen looks smoother.

7.2.5 Turbulent Propagation

Now, to obtain accurate strength turbulence on the beam, we need to calculate the total Fried parameter and divide it in each turbulent phase screen having a cumulative effect, in this way, we can obtain a weak and strong turbulence regime. Mathematically:

$$(7.30) \quad r_0 = \left(\sum_{i=1}^n r_{0_i}^{-5/3} \right)^{-3/5},$$

where,

$$(7.31) \quad r_{0_i} = [0.423k^2 C_{n_i} \Delta z_i]^{-3/5}.$$

Then, we can consider a propagation matrix $\chi_i = z_i/\Delta z_i$, and write the system as:

$$(7.32) \quad r_0^{-5/3} = \chi_i r_{0_i}^{-5/3},$$

the problem here is that $r_0^{-5/3}$ could have unphysical negative values, then, we need to make a computational optimization with this constraint.

Parameter	Value
λ	1.064e-6
$D_1 = D_2$	0.1
D_z	600
R	∞
ω_0	0.03
n_{screens}	20
$\delta_1 = \delta_n$	0.8e-3
N	2^9
l_0	0
L_0	∞
C_n^2	6.67e-15

Table 7.1: Table with the parameters used for the simulation.

As an example, we considered the parameters given in Table 7.1, which represents the propagation of 600 m through moderate-strong turbulence and we perform the turbulent propagation.

Fig. 7.8 a) shows the mode before propagation, and Fig. 7.8 b) shows the mode after turbulent propagation, we can observe how the intensity distribution of the propagated field reach higher values of intensity in certain regions, this is due the crosstalk, as a consequence, the scintillation is higher. Also, the phase of the propagated mode is unrecognizable, it is only possible to perceive the twist shape of the phase.

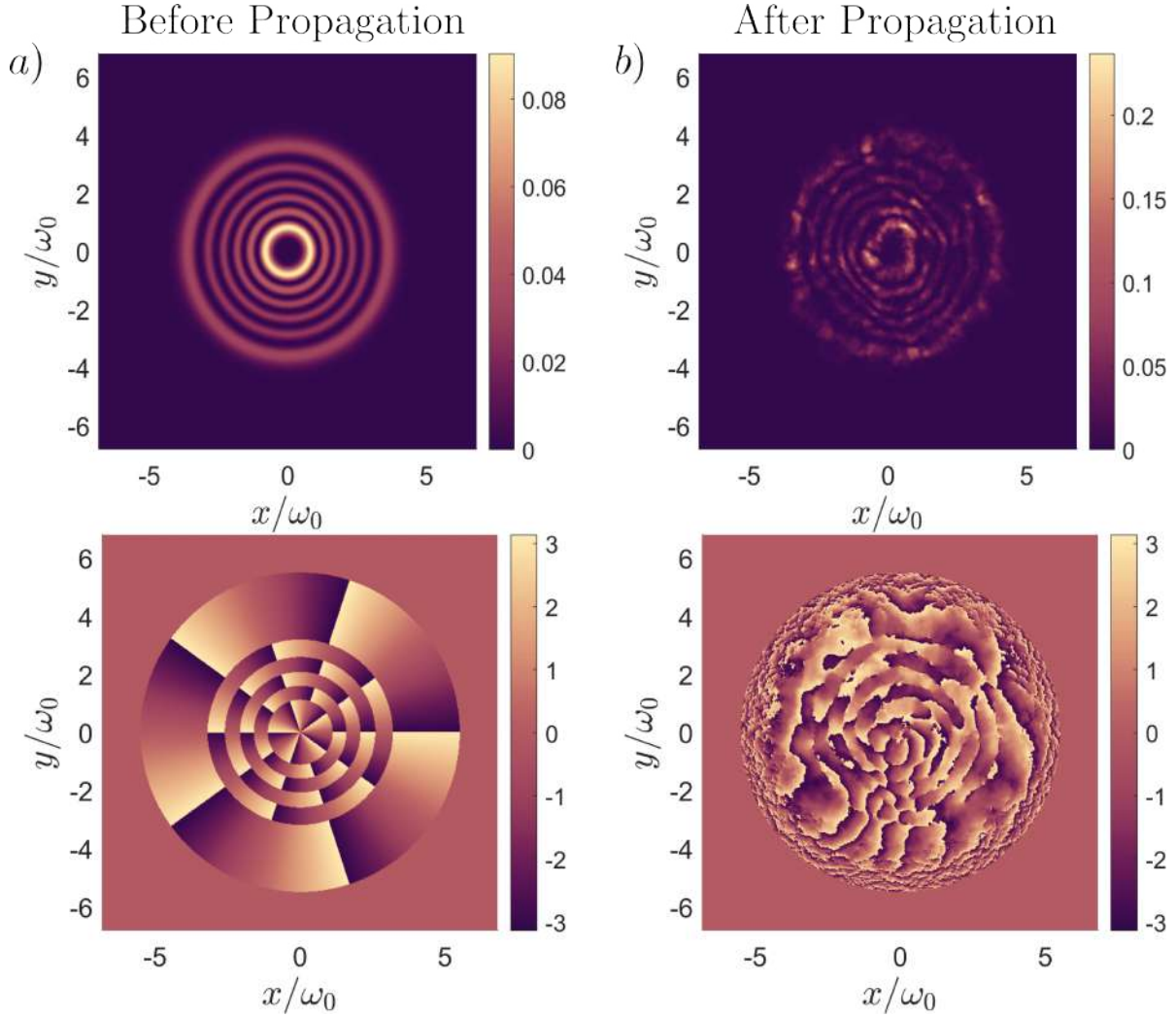


Figure 7.8: Turbulent propagation of LG mode with $l = 5$, $n = 5$. In a) the intensity and phase of the mode before propagation, in b) the intensity and phase after propagation.

7.2.6 Concurrence Calculation

To obtain the concurrence of the system, we first consider that each LG mode is a photon, then, we assume that the source generates a Bell state [67],

$$(7.33) \quad |\Psi\rangle = \frac{1}{\sqrt{2}} (|l\rangle_A |-l\rangle_B + |-l\rangle_A |l\rangle_B),$$

where the subscripts A and B are used to label two different paths of the two photons through turbulence. When a photon with a given OAM propagates through turbulence, the distortions cause the photon to become a superposition of many OAM modes. If we restrict the analysis over the basis $\{|-l_0, -l_0\rangle, |-l_0, l_0\rangle, |l_0, -l_0\rangle, |l_0, l_0\rangle\}$, then the state of the photon over a propagation distance Δz is of the form [67]:

$$\begin{aligned}
 |l\rangle_A &\rightarrow a_l |l\rangle_A + a_{-l} |-l\rangle_A, \\
 |-l\rangle_A &\rightarrow b_l |l\rangle_A + b_{-l} |-l\rangle_A, \\
 |l\rangle_B &\rightarrow c_l |l\rangle_B + c_{-l} |-l\rangle_B, \\
 |-l\rangle_B &\rightarrow d_l |l\rangle_B + d_{-l} |-l\rangle_B,
 \end{aligned}
 \tag{7.34}$$

where a_l, a_{-l} , and so on, are the complex coefficients in the expansion of the distorted state in terms of the OAM basis. Mathematically we can express them as the effect of the Turbulent operator, $U_{\Delta z}$, on the OAM state:

$$\begin{aligned}
 a_l &= \langle l|_A U_{\Delta z} |l\rangle_A, \\
 a_{-l} &= \langle -l|_A U_{\Delta z} |l\rangle_A, \\
 b_l &= \langle l|_A U_{\Delta z} |-l\rangle_A, \\
 b_{-l} &= \langle -l|_A U_{\Delta z} |-l\rangle_A, \\
 c_l &= \langle l|_B U_{\Delta z} |l\rangle_B, \\
 c_{-l} &= \langle -l|_B U_{\Delta z} |l\rangle_B, \\
 d_l &= \langle l|_B U_{\Delta z} |-l\rangle_B, \\
 d_{-l} &= \langle -l|_B U_{\Delta z} |-l\rangle_B.
 \end{aligned}
 \tag{7.35}$$

This is equivalent to apply the turbulent operator to the input state, $|\Psi\rangle$, as a result, the state is of the form [67]:

$$|\Psi\rangle_{\text{out}} = U_{\Delta z} |\Psi\rangle = C_1 |l\rangle_A |l\rangle_B + C_2 |l\rangle_A |-l\rangle_B + C_3 |-l\rangle_A |l\rangle_B + C_4 |-l\rangle_A |-l\rangle_B,
 \tag{7.36}$$

where,

$$\begin{aligned}
 C_1 &= \frac{1}{\sqrt{2}} (a_l d_l + b_l c_l) \\
 C_2 &= \frac{1}{\sqrt{2}} (a_l d_{-l} + b_l c_{-l}) \\
 C_3 &= \frac{1}{\sqrt{2}} (a_{-l} d_l + b_{-l} c_l) \\
 C_4 &= \frac{1}{\sqrt{2}} (a_{-l} d_{-l} + b_{-l} c_{-l}).
 \end{aligned}
 \tag{7.37}$$

The physical meaning of the coefficients a_l, b_{-l}, c_l, d_{-l} is the survival amplitude, and for the coefficients a_{-l}, b_l, c_{-l}, d_l is the crosstalk amplitude. Because we do not have a detailed knowledge of the medium, one needs to compute the ensemble average of the density matrix over a

representative set of instances of the medium, and due to the post-selection, the resulting density matrix must be normalized by its trace [62].

$$(7.38) \quad \rho = \frac{\sum_i^N |\Psi_i\rangle\langle\Psi_i|}{\text{Tr}\{\sum_i^N |\Psi_i\rangle\langle\Psi_i|\}},$$

where $|\Psi_i\rangle$ is the state of the qubit after the photons propagate through the i -th phase screen. Once we obtain the density matrix, we can obtain the concurrence by the methods described in 6.1.1.

It is important to recall that for HIG modes, we perform the same study, writing the Bell state for HIG modes in the same way that Bell state for LG modes, which is given by equation (7.33), this is:

$$(7.39) \quad |\Psi\rangle = \frac{1}{\sqrt{2}} (|HIG^+\rangle_A |HIG^-\rangle_B + |HIG^-\rangle_A |HIG^+\rangle_B),$$

where the $\{+, -\}$ corresponds to the rotating direction.

7.3 Numerical Results

In this section we present all our numerical results for LG and IG modes, the first section corresponds to LG modes, where we compare our results with the results of sections 7.2.2 and 7.1.3, once we corroborate our results with theirs, we investigate the IG modes.

7.3.1 Concurrence of Laguerre-Gauss modes Through Turbulence

Fig. 7.9 shows the comparison of the Numerical Simulation (NS), the Analytical Result (AR) [58, 63], and the two-photon wave mechanics theory (TWM) [60]. We observe that our numerical simulation has the same decay behavior as both theories, however, the Paterson theory has a higher decay, and the Smith and Rymer theory has a less decay, as discussed in section 7.1.3. The advantage of MPS is that it takes the effect of turbulence cumulatively, making it a more accurate theory. Also, theory predicts that the concurrence lasts longer for higher values of $|l|$, this is also true for our numerical simulation. This decay follows an exponential rule due to the dependence on the value l [63, 67]. These results have the same behavior as published results [59]. In this sense, we can say that our numerical simulation agrees with the theoretical and published results since they obtain the same decay behavior and the same decay scale. The MPS numerical simulation allows us to investigate the effect of turbulence in weak and strong turbulence regimes. This allows us to extend our analysis for different radial index values.

Fig. 7.10 shows the effect of turbulence on the entanglement for LG modes with a radial index different from zero. Our NS agrees with the Paterson model, in the sense that as the radial index increases, the resilience decreases. The decay is not so significant, and it is more distinguishable for low values of the azimuthal index. Also, we emphasize the fact that the radial index can be another information channel, increasing the data transmission capacity.

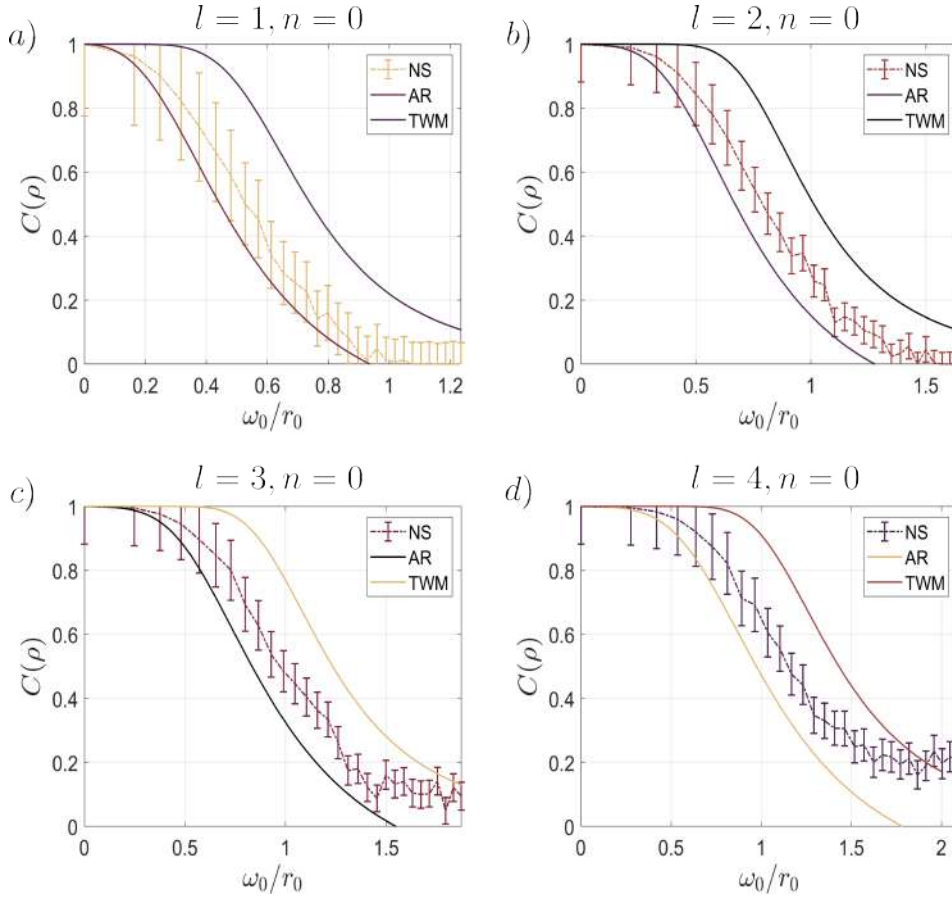


Figure 7.9: Concurrence comparison for AR, TWM, and NS. The numerical simulation has the same decay behavior as both theories. The analytical result describes a higher decay, while the TWM theory underestimates the effect of turbulence. Instead, the numerical simulation has a transition more in line with the cumulative effect of turbulence. Each point on the graph was averaged 1200 times.

7.3.2 Concurrence of Helicoidal Ince-Gauss modes Through Turbulence

Now we have corroborated our numerical simulation and extended the analysis to LG modes with a radial index different from zero. We investigate the concurrence of IG modes against turbulence, the idea here is to explore the effect of the ellipticity parameter against turbulence, to find the most resilient modes against turbulence. We carry out simulations for different values of order p , for each of these values, we carry out different values of degree m , and for each of these values, five values of ellipticity were used, $\varepsilon = \{0.0001, 1, 30, 200, 1000\}$. A representative set of graphs were chosen to demonstrate the phenomenon that we have observed. In Fig. 7.11 some values are shown. To understand the effect of the ellipticity on the concurrence for the HIG modes, we first plot the case $p = 1, m = 1$. This mode corresponds to the LG mode $l = 1, n = 0$. This is the reason why concurrence decays in the same way for all ellipticities, this confirms that our HIG modes

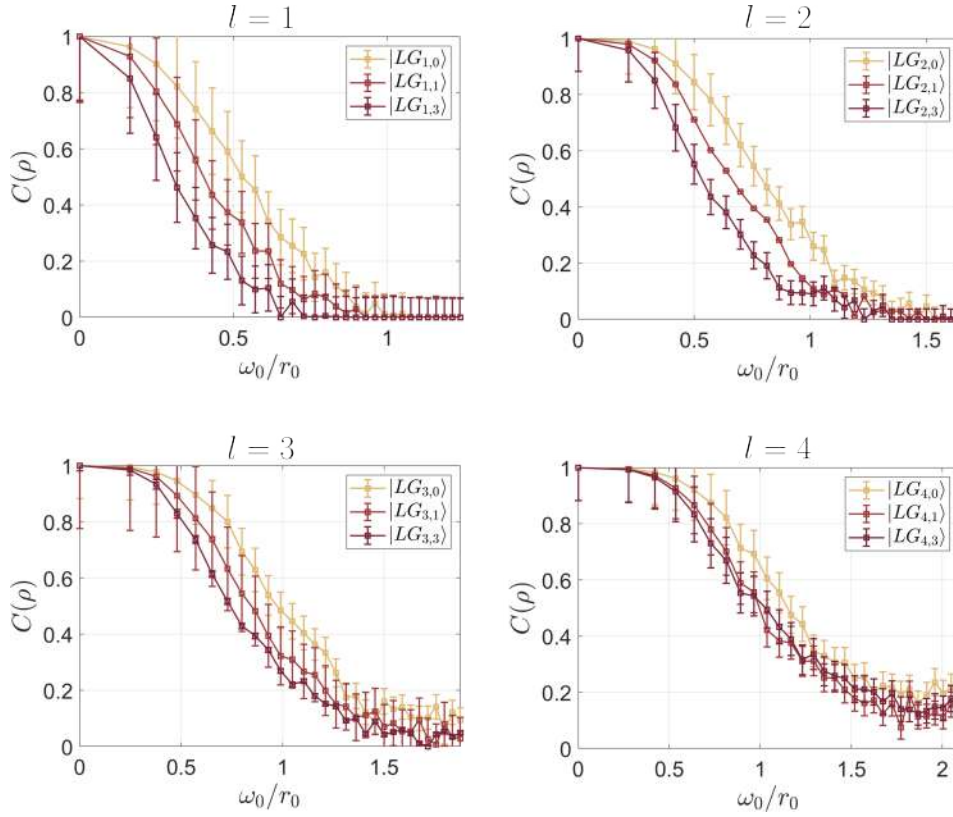


Figure 7.10: Effect of the turbulence on modes with a radial index different to zero, our NS agrees with Paterson model, as the radial number increases, the mode has less resilience, this phenomena are more distinguishable for low values of azimuthal number. Each point on the graph was averaged 1200 times.

have the same behavior when tending to a LG mode. We can also observe the intensity profile for different ellipticities, $\varepsilon = \{0.0001, 30, 200\}$. And in the case of $p = 1, m = 1$, all modes correspond to the same mode. Then, we analyze the effect of the degree m , for the same value of p . We consider $p = 3, m = 1$ and $p = 3, m = 3$, in the first case, we observe that the modes with greater ellipticity have a greater resilience to turbulence. Contrary case, when $p = 3, m = 3$ the modes with lower ellipticity have a greater resilience to turbulence. To exclude that this behavior was only exclusive to this mode, we analyzed different modes following the same principle, we choose a p value and we change the m value with the same ellipticities. We plot the modes $p = 15, m = \{1, 7, 15\}$. Again, for $m = 1$, modes with higher ellipticity are more resilient to turbulence than modes with lower ellipticity. However, when $m = 7$, the modes with lower ellipticity are slightly more resilient than the modes with higher ellipticity, it could be considered that due to error uncertainty, it is not clear which mode is more resilient, but it is possible to affirm that the modes with less ellipticity have increased their resilience. Finally, when $m = p = 15$, the modes with lower ellipticity are more resilient than the modes with higher ellipticity. We notice that the effect of ellipticity is not so significant for resilience for turbulence, but the fact that the mode has cylindrical symmetry

and tends to be an LG mode.

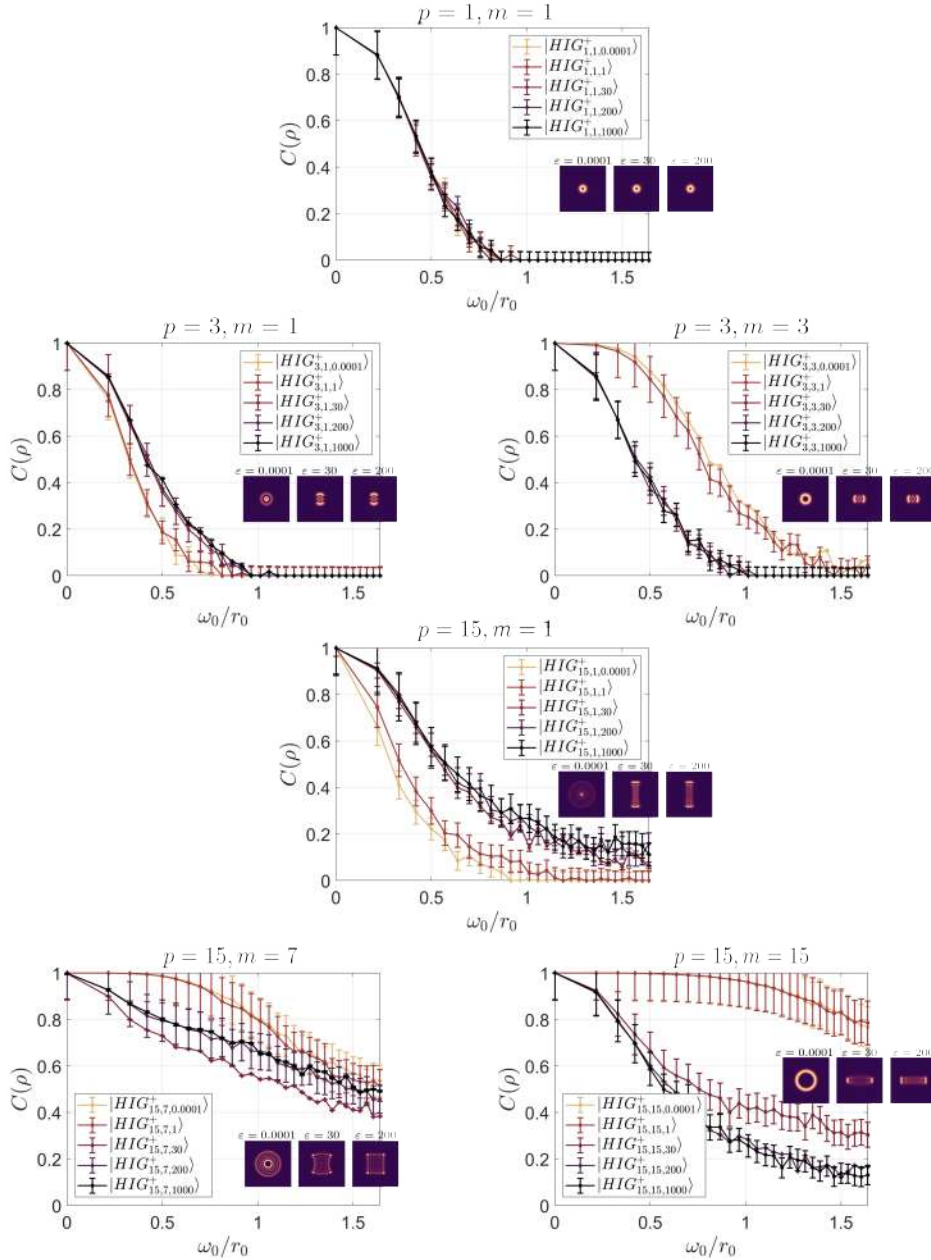


Figure 7.11: Concurrence for a representative set of HIG. The mode $p = 1, m = 1$, corresponds to a LG with $l = 1, n = 0$, for this reason, the concurrence decays identical for each ellipticity. In the case of $p = 3, m = 1, 3$ there is high resilience for low ellipticities in the case $m = 3$. For a mode with a high value of $p = 15$, and different values of $m = 1, 7, 15$ same phenomenon is observed, the low ellipticities have less resilience until $m = 7$, at this point all ellipticities present similar resilience when m increases the low ellipticities have higher resilience respect to high ellipticities. Each point in the graph was averaged 1800 times.

EXPERIMENTAL SETUP

To verify our numerical results, we develop an experimental setup in which we corroborate the theoretical spiral bandwidth, to validate the correlation between photons. After that, we effectuated quantum state tomography to reconstruct the density matrix and obtain the concurrence of each point. Fig. 8.1 shows the experimental setup used.

We use a Moglab Diode Laser of 405 nm to generate photon pairs at 810 nm using SPDC in collinear geometry. The lens L_1 is an aspheric lens of 5 mm focal distance, and the L_2 lens is a triplet that generates a Gaussian mode. The BG39 cleans the second harmonic of the laser. After that, the L_3 lens with a focal distance of 1000 mm focuses the pump onto the BBO with a power of 30 mW. After the BBO crystal, a high pass filter, and a 5 nm band pass filter were used to filter out the pump light and only transmit photons with 810 nm. The lenses L_4 , L_5 with 300 mm and 120 mm focal distance, respectively, form a $2.5\times$ magnifying telescope, which maps the image plane of the BBO crystal into the PLUTO-2.1 Spatial Light Modulator (SLM). Then, the image of the SLM is mapped into the APDs by two demagnifying telescopes T_1 and T_2 . The telescope T_1 consists of two lenses of 100 mm and 250 mm, respectively, which demagnify by $2.5\times$. Finally, a telescope T_2 consists of two lenses of 500 mm and 9 mm, respectively, which allows us to couple to a single mode fiber and have a coincidence detection in the APDs.

In detail, the experimental setup consists of three phases, the first phase is the generation of photon pairs at a wavelength of 810 nm by the incidence of the beam into the BBO crystal and the SPDC phenomenon. The second phase is the spatial discrimination of the spatial modes. This is done through three main elements, the KEM, which allows us to divide the SLM screen in two, one for each photon. The spatial light modulator, which generates the corresponding phase in the incident mode, and the single-mode fiber, which allows the detection of a single mode. The third phase is coincidence detection, which is done using APDs. Specifically, the incidence to the SLM

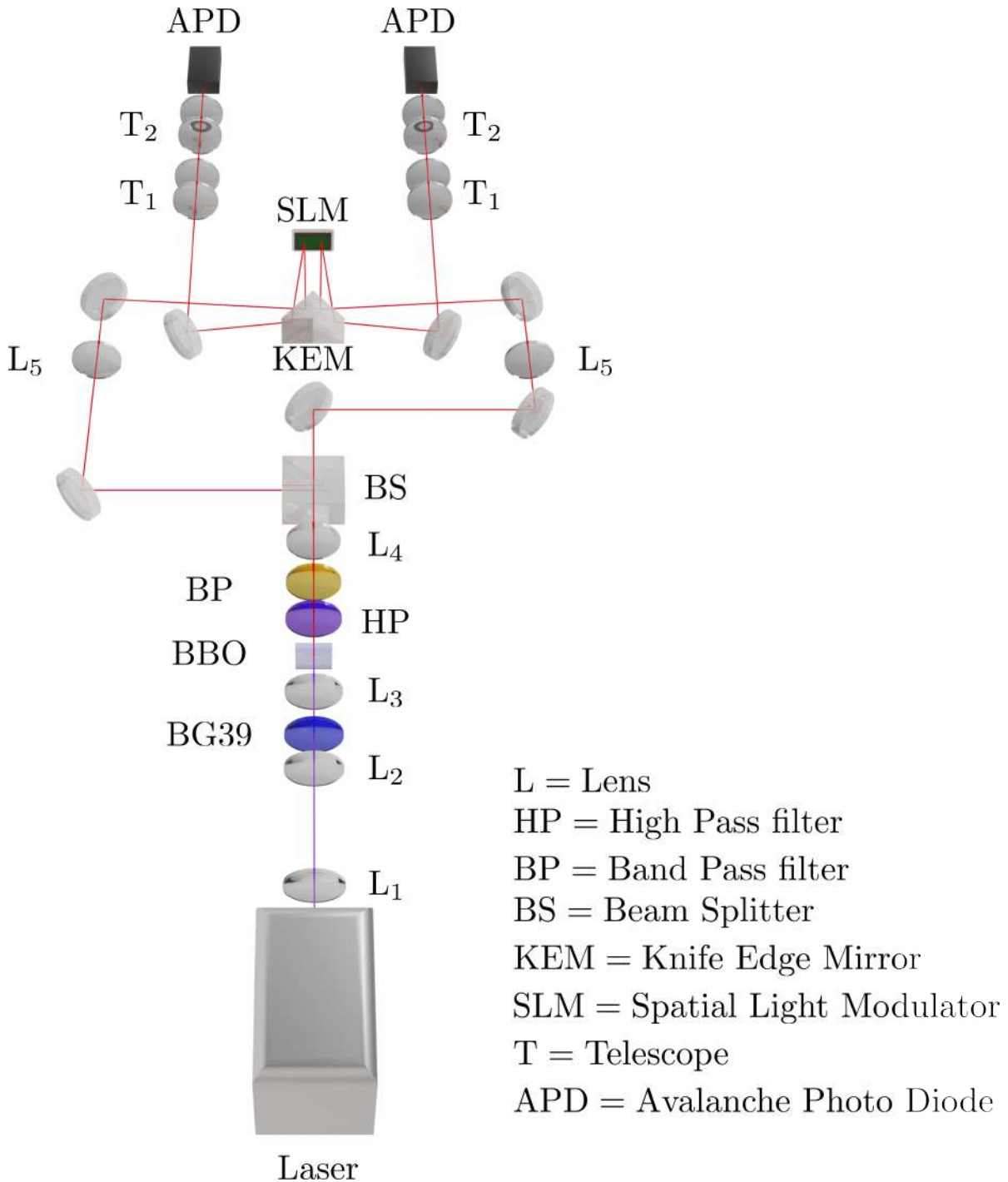


Figure 8.1: Experimental setup for a photon pair generation. A detailed description of the setup is in the text.

must be with an angle no greater than 7 degrees and with horizontal polarization.

8.1 Digital Masks on the SLM

To spatially modulate light, it is necessary to generate digital masks that are projected onto the SLM. Different methods can be found in the literature, we follow these works [78, 79]. The idea is to sum a linear grating, which diffracts the beam, and the phase of the mode of interest, modulate the resultant mask by a sin factor, and multiply it by the inverse Bessel function of the first kind, J_1^{-1} at the value 0.58. Fig. 8.2 shows in an illustrative way how to form a only phase mask.

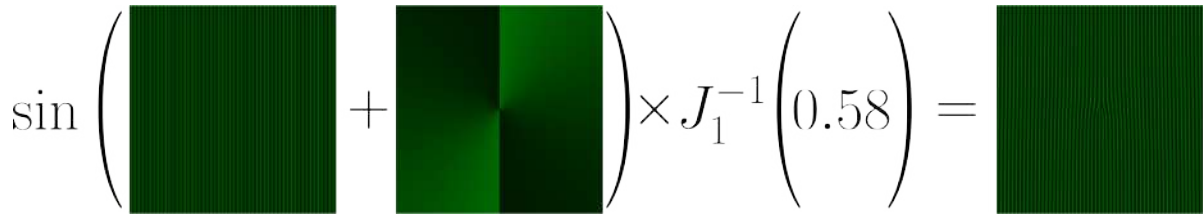
$$\sin \left(\text{img1} + \text{img2} \right) \times J_1^{-1}(0.58) = \text{img3}$$


Figure 8.2: The process to generate a phase-only digital mask for the SLM.

If we want to modulate the amplitude, we can add the amplitude factor to the inverse Bessel function, also, if we want a turbulent mask, the phase turbulent factor must be added to the phase of the beam. Fig. 8.3 shows the comparison of a generation of a mask without turbulence and a mask with turbulence.

$$\sin \left(\text{img1} + \text{img2} \right) \times J_1^{-1}(0.58) = \text{img3}$$

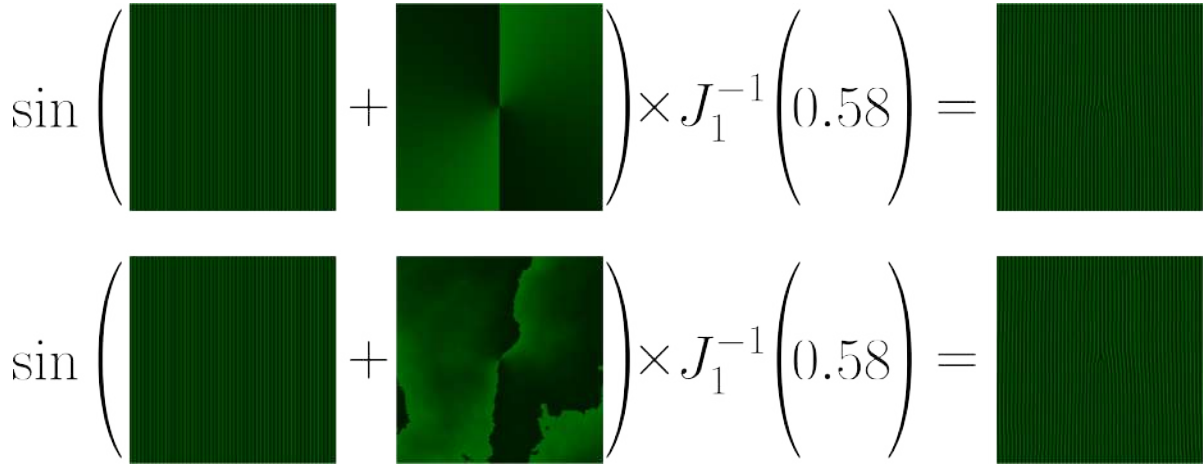
$$\sin \left(\text{img1} + \text{img4} \right) \times J_1^{-1}(0.58) = \text{img5}$$


Figure 8.3: The comparison of a generation of a mask without turbulence and a mask with turbulence. The effect of the turbulence is projected on the diffraction effect, as the turbulence strength increases, fewer counts in coincidence are obtained, this effect is the crosstalk of the OAM.

It is important to recall, that the correct alignment of the masks is an important characteristic

since the lateral displacement of the masks induces overlapping of modes, obtaining undesired correlations.

8.2 Quantum State Tomography

Quantum state tomography (QST) is a technique that allows to reconstruct the density matrix of the system. Since it is in principle impossible to determine the state of an unknown quantum system if only one has a single copy of the state. This is because there is no quantum measurement that can accurately distinguish non-orthogonal states [80].

To be explicit, we will follow the work of [81, 82] and as an example, we will perform quantum state tomography for the bell state $|\psi\rangle = (1/\sqrt{2})(|l\rangle_A |-l\rangle_B + |-l\rangle_A |l\rangle_B)$. First, we consider a set basis, in our case, we take the next basis:

$$(8.1) \quad |H\rangle = \begin{bmatrix} 1 \\ 0 \end{bmatrix}, \quad |V\rangle = \begin{bmatrix} 0 \\ 1 \end{bmatrix}, \quad |D\rangle = \frac{1}{\sqrt{2}}(|H\rangle + |V\rangle), \quad |L\rangle = \frac{1}{\sqrt{2}}(|H\rangle - i|V\rangle),$$

where, $|H\rangle$ corresponds to $|l\rangle$ and $|V\rangle$ corresponds to $|-l\rangle$. Once the basis is defined, 16 measurements can be done, and we can describe our state as:

$$(8.2) \quad |\psi_\nu\rangle = |\varphi\rangle \otimes |\varphi\rangle,$$

where the index ν describes each measurement, therefore, $\mu = 1, \dots, 16$, and $|\varphi\rangle$ is defined as:

$$(8.3) \quad |\varphi\rangle = \begin{bmatrix} H \\ V \\ D \\ L \end{bmatrix}.$$

Consequently, the average number of coincidence counts that will be observed in a given experimental run is [82]:

$$(8.4) \quad n_\nu = N \langle \psi_\nu | \hat{\rho} | \psi_\nu \rangle,$$

where N is a constant dependent on the photon flux and detection efficiency. Then, we can express the tomographic reconstruction of the density matrices of our states [82]:

$$(8.5) \quad \hat{\rho} = \frac{\sum_{\nu=1}^{16} \hat{M}_\nu n_\nu}{\sum_{\nu=1}^4 n_\nu},$$

where the \hat{M}_ν matrices are explicitly described in [82]. In our case, considering the 5% of photon fluctuation, the counts are $n_1 = 0$, $n_2 = 298$, $n_3 = 205$, $n_4 = 218$, $n_5 = 492$, $n_6 = 0$, $n_7 = 180$, $n_8 = 190$, $n_9 = 179$, $n_{10} = 154$, $n_{11} = 346$, $n_{12} = 120$, $n_{13} = 188$, $n_{14} = 191$, $n_{15} = 110$, $n_{16} = 368$.

After apply equation (8.5) we obtain:

$$(8.6) \quad \hat{\rho} = \begin{bmatrix} -0.0875 & 0.3076 - 0.4472i & -0.9528 - 0.3569i & 0.8444 - 0.2396i \\ 0.3076 + 0.4472i & 0.5875 & 0.2000 + 0.4562i & -0.2444 + 1.0264i \\ -0.9528 + 0.3569i & 0.2000 - 0.4562i & 0.4847 & 1.0174 - 0.1958i \\ 0.8444 + 0.239i & -0.2444 - 1.0264i & 1.0174 + 0.1958i & 0.0153 \end{bmatrix}.$$

This matrix is by definition normalized and Hermitian, but doesn't have the property of positive semidefiniteness [82]. To solve this, we must apply another technique known as Maximum Likelihood Estimation. This method is described in [82]. After that, the density matrix for our example is:

$$(8.7) \quad \hat{\rho} = \begin{bmatrix} 0.0021 & -0.0110 - 0.0020i & -0.0085 + 0.0053i & 0 \\ -0.0110 + 0.0020i & 0.4926 & 0.4737 + 0.0112i & -0.0094 + 0.0062i \\ -0.0085 - 0.0053i & 0.4737 - 0.0112i & 0.5050 & -0.0098 + 0.0069i \\ 0 & -0.0094 - 0.0062i & -0.0090 - 0.0069i & 0.0002 \end{bmatrix}.$$

This matrix does have a physical meaning. Fig. 8.4 shows the graphical representation of the density matrix, which agrees with the values expected for a Bell state.

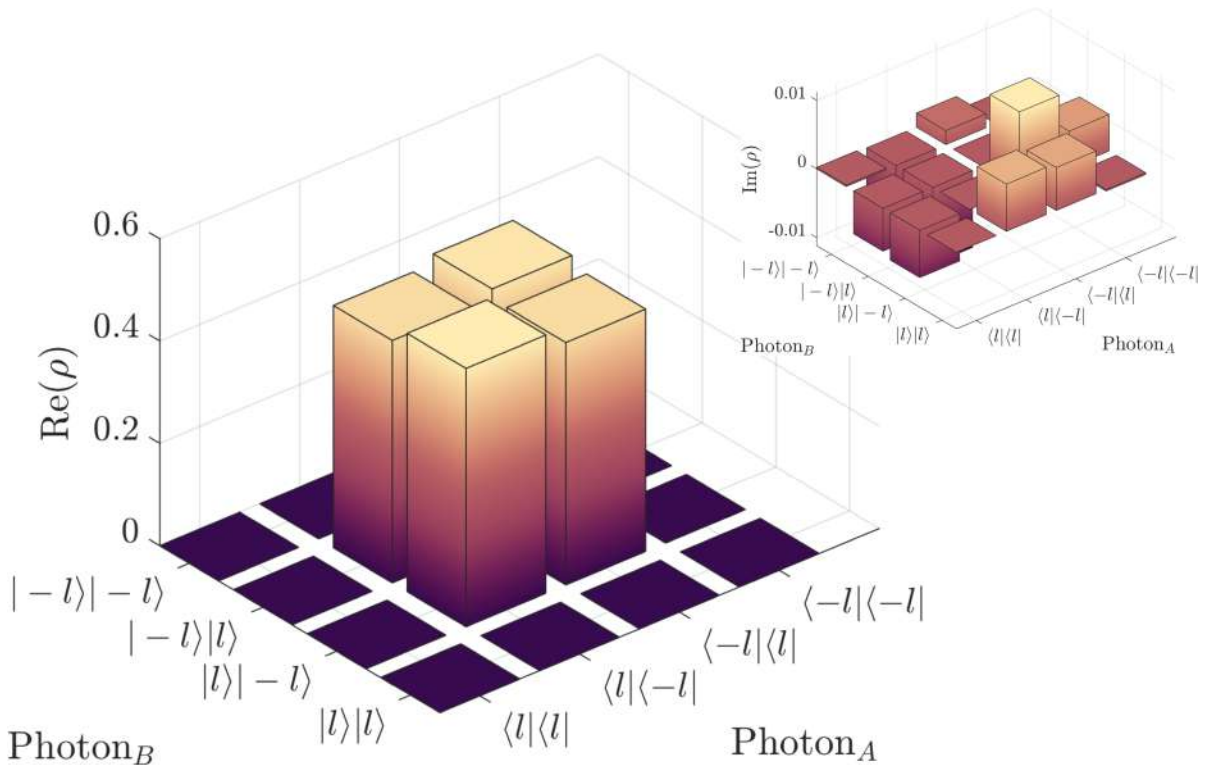


Figure 8.4: Graphical visualization of the density matrix obtained by Maximum Likelihood Estimation.

Once the density matrix is calculated, we can obtain the concurrence as previously described in 6.1.1. We obtain the following eigenvalues: $\lambda_1 = 0.9452$, $\lambda_2 = 0.0006$, $\lambda_3 = \lambda_4 = 0$. Then, the concurrence has a value of $C(\rho) = 0.9472 \pm 0.1636$.

For the case of mixed states, i.e., states with non-zero turbulence, an average of measurements must be taken, that is, measured with different turbulence masks, and therefore, apply QST to the count average.

RESULTS AND CONCLUSIONS

In this Chapter we present our results. First, we compare the theoretical and experimental spiral bandwidth. After that, we compare our numerical simulations and our experimental results. The results are divided into two sections, the first one corresponds to the LG concurrence, and the second, corresponds to the HIG concurrence.

9.1 Experimental Spiral Bandwidth

We measured the spiral bandwidth to corroborate the OAM correlation of the two photons. Fig. 9.1 a) shows the comparison between the theoretical model and the spiral bandwidth measurements. For this case, the correlations in OAM between photons A and B with respect to the normalized weight are shown. Also, the experimental correlation is shown. Both correlations show the same distribution, so it is possible to determine the γ factor. For this case the fit yields a value of $\gamma = 1.82$. In Fig. 9.1 b) shows the theoretical distribution for $\gamma = 1.82$, we can see that the distribution obtained theoretically adapts correctly to the experimental distribution for this experimental setup configuration according to equation (5.10).

9.2 Experimental Concurrence of Laguerre-Gauss modes

We measured the LG modes with zero radial index. Fig. 9.2 a) shows the LG modes with $l = 1$ and $l = 3$. We observe that our numerical simulation and experimental results agree. We choose to plot $l = \{1,3\}$ to observe the difference in the resilience of the modes, as we previously discussed, as l increases, the mode is more resilient. Each point in the graph was averaged 40 times, and we take 30 points to show the decay more clearly. There is a small discrepancy for the points corresponding to higher scintillation due to the difficulty of measuring with masks with high turbulence, that is,

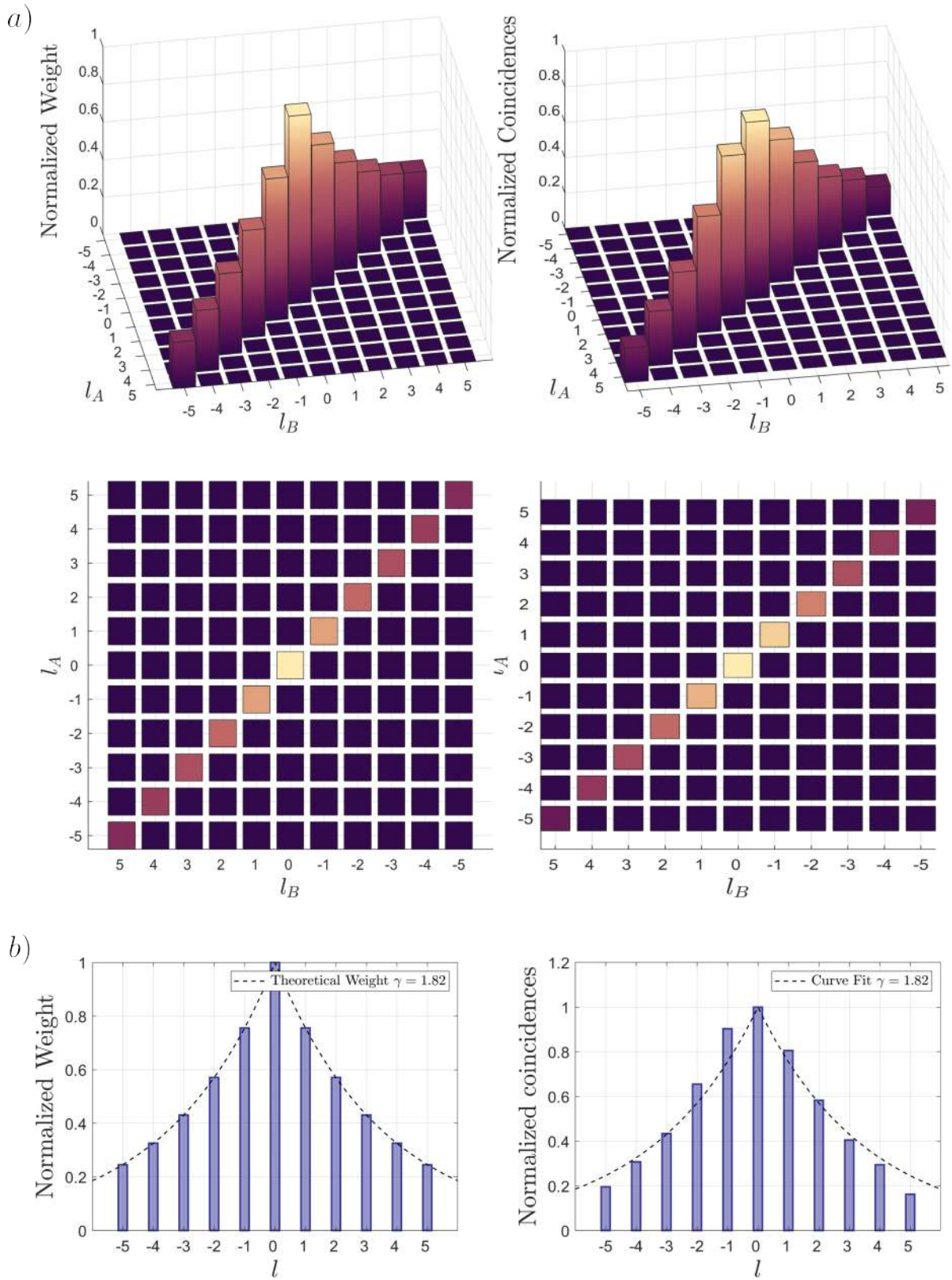


Figure 9.1: Comparison between theoretical spiral bandwidth and experimental spiral bandwidth. In a) the experimental correlation between OAM values agrees with the theoretical correlation. In b) we find the γ value.

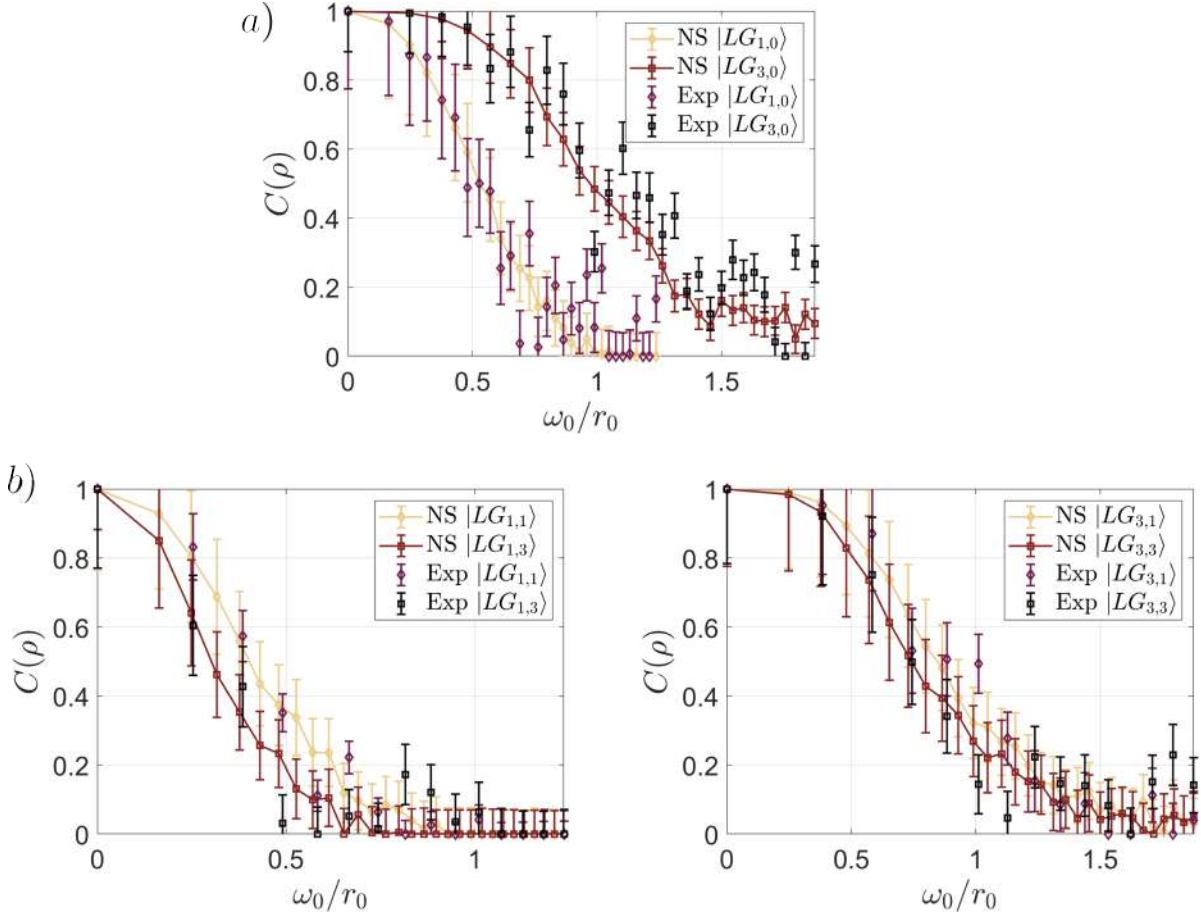


Figure 9.2: Comparison between numerical simulation and experimental measurements for LG modes. The measurements agree with the numerical simulation. Each point was averaged 40 times.

masks that present greater deformation. In Fig. 9.2 b), we show the measurements for a non-zero radial index, in this case, we choose $l = 1$, and $l = 3$, with radial indices $n = 1$, $n = 3$. The decay generated by the non-zero radial index does not present a significant loss and has the advantage that the radial index can be used as another channel, increasing the transmission capacity.

9.3 Experimental Concurrence of Helicoidal Ince-Gauss modes

Similarly, we compare our numerical simulations of HIG modes, with the experimental results. In this case, we choose to plot two values of ellipticity for each mode, $\varepsilon = \{0.0001, 200\}$, the reason why we chose these values, was, first, to obtain a greater contrast between the low and high ellipticities depending on the degree m , and second, to not saturate the graph with all the values of the ellipticity. First, we measured the mode $p = 1$, $m = 1$, which agrees with the numerical simulation. After that, we measured the modes $p = 3$, $m = \{1, 3\}$, and we can observe how the

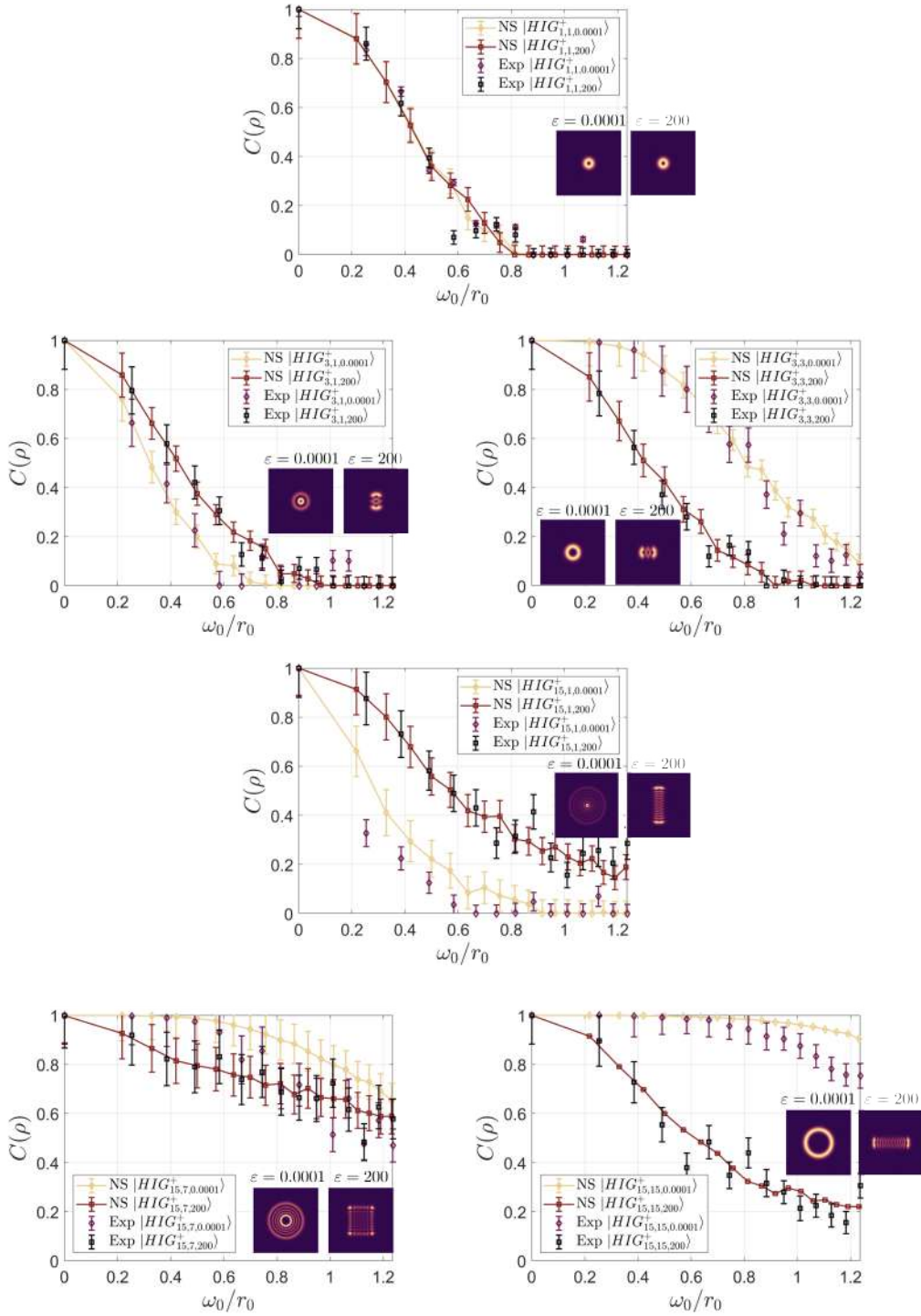


Figure 9.3: Comparison between numerical simulation and experimental measurements for HIG modes. The measurements follow the same pattern as NS, and the data agree with NS. Each point was averaged 40 times.

experimental data follows the same pattern observed in the numerical result, the fact of choosing a low ellipticity value and a high one, perfectly shows the dependence of the degree m and the ellipticity. Finally, we measured the modes $p = 15$, $m = \{1, 7, 15\}$, In these modes the transition of the resilience for modes with low ellipticities is clearly shown, which implies that the modes with cylindrical symmetry have a greater resilience with respect to turbulence, and in general, when the HIG modes tend to be LG modes, the resilience is maximum, that is, when $p = m$. The data points agree with the numerical simulation, corroborating the effectiveness and validity of the numerical simulation and the experimental setup. Each data point was averaged 40 times.

9.4 Conclusions

In Chapter 1, the main motivation for this work was discussed. Then, from Chapters 2 to 6, the necessary bases in the theoretical framework to understand this work were presented.

In Chapter 7 we corroborate the validity of the numerical simulation with respect to two theories based on SPS, the numerical simulation correctly showed the behavior of entanglement with respect to scintillation, in addition, the numerical results were corroborated with the literature. Demonstrating in the case of the LG modes that the modes with the highest OAM are more appropriate for propagation in turbulence, in addition, it was demonstrated that for values of the radial index different from zero, the concurrence does not present a significantly greater decay, being possible to use this quantity as another channel in the transmission of information. In the case of the HIG modes, it was shown that the effect of ellipticity is dependent on the degree m , as the value of m increases, the modes with low ellipticity are more resilient, that is, when the HIG modes tend to be LG modes.

In Chapter 8 the experimental development was discussed, also the generation of digital masks to measure the correlation of photons in OAM and how to calculate the concurrence using QST.

In Chapter 9 it was shown that the experimental results agree with the numerical simulations, concluding that the effect of turbulence is basis dependent. However, it is emphasized that it is necessary to make a more realistic numerical model and confirm this by measurements outside the laboratory, which represents a greater challenge but would demonstrate the precise effect of turbulence on entanglement with OAM.

REFERENCIAS

- [1] Bennett C. H. and Brassard G. “*Quantum cryptography: Public key distribution and coin tossing.*”, *arXiv:2003.06557 [quant-ph]*, 1984.
- [2] Pan J.-w. “*Quantum science satellite.*”, *Chin. J. Sp. Sci.* **34**, 547–549, 2014.
- [3] Misiaszek–Schreyner M. “*Applications of single-photon technology.*”, *arXiv:2205.10221 [quant-ph]*, [Doctoral dissertation], 2022.
- [4] Bedington R., Arrazola J. M. and Ling, A. “*Progress in satellite quantum key distribution.*”, *npj Quantum Inf* **3**, 30, 2017.
- [5] Siegman A. E. “*Lasers.*”, *Universe Science Books*, 1986.
- [6] Allen L., Beijersbergen M. W., Spreeuw R. J. C., and Woerdman J. P. “*Orbital angular momentum of light and the transformation of Laguerre-Gaussian laser modes.*”, *Phys. Rev. A* **45**, 8185, 1992.
- [7] Bandres M. A., and Gutiérrez-Vega J. C. “*Ince–Gaussian modes of the paraxial wave equation and stable resonators.*”, *J. Opt. Soc. Am. A* **21**, 873-880, 2004.
- [8] O’Neil A. T. and Padgett M. J. “*Three-dimensional optical confinement of micron-sized metal particles and the de-coupling of the spin and orbital angular momentum within an optical spanner.*”, *Opt. Commun.* **185**, 139-143, 2000.
- [9] Gahagan K. T. and Schwartzlander G. A. “*Optical vortex trapping of particles.*”, *Opt. Lett.* **21**, 827-9, 1996.
- [10] Calvo G. F., Picon A., and Bagan E. “*Quantum field theory of photons with orbital angular momentum.*”, *Phys. Rev. A* **73**, 013805, 2006.
- [11] Plick W. N. and Krenn M. “*Physical meaning of the radial index of Laguerre-Gauss beams.*”, *Phys. Rev. A*, **92**, 063841, 2015.
- [12] Ebrahim K., Giovannini D., Bolduc E., Bent N., Miatto F. M., Padgett M. J., and Boyd R. W. “*Exploring the quantum nature of the radial degree of freedom of a photon via Hong-Ou-Mandel interference.*”, *Phys. Rev. A* **89**, 013829, 2014.

-
- [13] Arscott F. M. “*Periodic Differential Equations.*”, Pergamon, Oxford, UK, 1964.
- [14] Arscott F. M. “*The Whittaker-Hill equation and the wave equation in paraboloidal coordinates.*”, *Proc. R. Soc. Edinburgh Sect. A* 67, 265–276, 1967.
- [15] Bandres M. A. and Gutiérrez-Vega J. C. “*Ince–Gaussian beams.*”, *Opt. Lett.* 29, 144–146, 2004.
- [16] Boyer C. P., Kalnins E. G., and Miller W. Jr. “*Lie theory and separation of variables. 7. The harmonic oscillator in elliptic coordinates and the Ince polynomials.*”, *J. Math. Phys.* 16, 512–523, 1975.
- [17] Plick W. N., Krenn M., Fickler R., Ramelow S., and Zeilinger A. “*Quantum orbital angular momentum of elliptically symmetric light.*”, *Phys. Rev. A* 87, 033806, 2013.
- [18] Obukhov A. M. “*On the spectrum of isotropic temperature fluctuations in an isotropic turbulence.*”, *Izv. Acad. Nauk. SSSR, Ser. Geogr. I Geofiz.*, 13, 1949
- [19] Larry C. A. and Ronald L. P. “*Laser Beam Propagation through Random Media.*”, *SPIE PRESS BOOK, 2nd Edition*, 2005.
- [20] Djordjevic I. B. “*Deep-space and near-Earth optical communications by coded orbital angular momentum (OAM) modulation.*”, *Opt. Express* 19, 14277–14289, 2011.
- [21] Amhoud E. M., Trichili A., Ooi B. S. and Alouini M. S. “*OAM Mode Selection and Space–Time Coding for Atmospheric Turbulence Mitigation in FSO Communication.*”, *IEEE Access*, 7, pp. 88049–88057, 2019.
- [22] Kolmogorov A. N. “*The local structure of turbulence in an incompressible viscous fluid for very large reynolds numbers.*”, *C. R. (Doki) Acad. Sci. U.S.S.R.*, 30, pp. 301–305, 1922.
- [23] Ricker D. W. “*Echo signal processing.*”, Springer, 2003.
- [24] Wheelon A. D. “*Electromagnetic Scintillation.*”, Cambridge, U.K.: Cambridge University Press, 2004.
- [25] Reinhardt G. W. and Collins Jr. S. A. “*Outer-scale effects in turbulence-degraded light-beam spectra.*”, *J. Opt. Soc. Am.* 62, 1526–1528, 1972.
- [26] Tatarski V. I. “*Wave Propagation in a Turbulent Medium.*”, McGraw-Hill, 1961.
- [27] Voitikhovich V. V. “*Outer scale of turbulence: comparison of different models.*”, *J. Opt. Soc. Am. A* 12, 1346–1353, 1995.
- [28] Goodman J. W. “*Statistical Optics.*”, Wiley and Sons, 1985.

-
- [29] Ishimaru A. “*Wave Propagation and Scattering in Random Media.*”, Wiley-IEEE Press, New York, 1999.
- [30] Clifford S. F. “*Laser Beam Propagation in the Atmosphere, ch. The Classical Theory of Wave Propagation in the Atmosphere*”, Springer-Verlag, 1978.
- [31] Sasiela R. J. “*Electromagnetic Wave Propagation in Turbulence: Evaluation and Application of Mellin Transforms*”, 2nd Ed., SPIE Press, 2007.
- [32] Fried D. L. “*Statistics of a geometric representation of wavefront distortion*”, *J. Opt. Soc. Am.* 55(11), pp. 1427-1431, 1965.
- [33] Louisell W. H., Yariv A. and Siegman A. E. “*Quantum fluctuations and noise in parametric processes I.*”, *Phys. Rev.*, 124, 1646–1654, 1961.
- [34] Burnham D. C. and Weinberg D. L. “*Observation of simultaneity in parametric production of optical photon pairs.*”, *Phys. Rev. Lett.*, 25, 84–87, 1970.
- [35] Kwiat P. G. , Mattle K., Weinfurter H., Zeilinger A., Sergienko A. V., and Shih Y. “*New High-Intensity Source of Polarization-Entangled Photon Pairs.*”, *Phys. Rev. Lett.*, 75, 4337, 1995.
- [36] Mair A., Vaziri A., Weihs G. and Zeilinger A. “*Entanglement of the orbital angular momentum states of photons.*”, *Nature* 412, 313–316, 2001.
- [37] Pittman T. B., Shih Y. H., Strekalov D. V. and Sergienko A. V. “*Optical imaging by means of two-photon quantum entanglement.*”, *Phys. Rev. A.*, 52, R3429, 1995.
- [38] Lindner C., Kunz J., Herr S. J., Wolf S., Kießling J. and Kühnemann F. “*Nonlinear interferometer for Fourier-transform mid-infrared gas spectroscopy using near-infrared detection*”, *Opt. Express*, 29, 4035, 2021.
- [39] Vanselow A., Kaufmann P., Zorin I., Heise B., Chrzanowski H. M. and Ramelow S. “*Frequency-domain optical coherence tomography with undetected mid-infrared photons.*”, *Optica*, 7, 1729, 2020.
- [40] Kutas M., Haase B., Bickert P., Riexinger F., Molter D. and von Freymann G. “*Terahertz quantum sensing.*”, *Sci. Adv.*, 6, 11, 2020.
- [41] Boyd R. “*Nonlinear Optics*”, Academic Press, Third Edition, 2008.
- [42] Loudon R. “*The quantum theory of light*”, Oxford: Oxford University Press, Third Edition, 2000.

- [43] Gatti A., Brambilla E., Caspani L., Jedrkiewicz O., and Lugiato L. A. “X Entanglement: The Nonfactorable Spatiotemporal Structure of Biphoton Correlation.”, *Phys. Rev. Lett.* 102, 223601, 2009.
- [44] Brambilla E., Caspani L., Lugiato L. A. and Gatti A. “Spatiotemporal structure of biphoton entanglement in type-II parametric down-conversion.”, *Phys. Rev. A* 82, 013835, 2010.
- [45] Mair A., Vaziri A., Weihs G. et al. “Entanglement of the orbital angular momentum states of photons.”, *Nature* 412, 313–316, 2001.
- [46] Vaziri A., Weihs G. and Zeilinger A. “Experimental Two-Photon, Three-Dimensional Entanglement for Quantum Communication”, *Phys. Rev. Lett.* 89, 240401, 2002.
- [47] Gröblacher S. et al. “Experimental quantum cryptography with qutrits”, *New J. Phys.* 8, 75, 2006.
- [48] Torres J. P., Alexandrescu A. and Torner L. “Quantum spiral bandwidth of entangled two-photon states”, *Phys. Rev. A* 68, 050301(R) 2003.
- [49] Bahaa E. A. S., Ayman F. A., Sergienko A. V. and Teich M. C. “Duality between partial coherence and partial entanglement”, *Phys. Rev. A* 62, 043816, 2000.
- [50] Miatto F. M., Yao A. M. and Barnett S. M. . “Full characterization of the quantum spiral bandwidth of entangled biphotons”, *Phys. Rev. A* 83, 033816, 2011.
- [51] Einstein A., Podolsky B. and Rosen N. “Can Quantum-Mechanical Description of Physical Reality Be Considered Complete?”, *Phys. Rev.* 47, 777, 1935.
- [52] Bell J. S. “On the Einstein Podolsky Rosen paradox”, *Physics Physique Fizika* 1, 195, 1964.
- [53] Werner R. F. “Quantum states with Einstein-Podolsky-Rosen correlations admitting a hidden-variable model”, *Phys. Rev. A* 40, 4277, 1989.
- [54] Braunstein S. L., Mann A. and Revzen M. “Maximal violation of Bell inequalities for mixed states”, *Phys. Rev. Lett.* 68, 3259, 1992.
- [55] Hill S. A. and Wootters W. K. “Entanglement of a Pair of Quantum Bits”, *Phys. Rev. Lett.* 78, 5022, 1997.
- [56] Wootters W. K. “Entanglement of Formation of an Arbitrary State of Two Qubits”, *Phys. Rev. Lett.* 80, 2245, 1998.
- [57] Uhlmann A. “Fidelity and concurrence of conjugated states”, *Phys. Rev. A* 62, 032307, 2000.
- [58] Paterson C. “Atmospheric Turbulence and Orbital Angular Momentum of Single Photons for Optical Communication.”, *Phys. Rev. Lett.* 94, 153901, 2005.

- [59] Leonhard N., Sorelli G., Shatokhin V. N., Reinlein C. and Buchleitner A. “*Protecting the entanglement of twisted photons by adaptive optics.*”, *Phys. Rev. A* 97, 012321, 2018.
- [60] Smith B. J. and Raymer M. G. “*Two-photon wave mechanics.*”, *Phys. Rev. A* 74, 062104, 2006.
- [61] Gonzalez A. J. R. and Brun T. A. “*Protecting orbital-angular-momentum photons from decoherence in a turbulent atmosphere.*”, *Phys. Rev. A* 88, 022326, 2013.
- [62] Bertlmann R. A., Durstberger K. and Hiesmayr B. C. “*Decoherence of entangled kaons and its connection to entanglement measures.*”, *Phys. Rev. A* 68, 012111, 2003.
- [63] Leonhard N. D., Shatokhin V. N. and Buchleitner A. “*Universal entanglement decay of photonic-orbital-angular-momentum qubit states in atmospheric turbulence.*”, *Phys. Rev. A* 91, 012345, 2015.
- [64] Doster T. and Watnik A. T. “*Laguerre–Gauss and Bessel–Gauss beams propagation through turbulence: analysis of channel efficiency.*”, *Appl. Opt.* 55, 10239–10246, 2016.
- [65] Frehlich R. “*Simulation of laser propagation in a turbulent atmosphere.*”, *Appl. Opt.* 39, 393–397, 2000.
- [66] Nelson W., Palastro J. P., Davis C. C. and Sprangle P. “*Propagation of Bessel and Airy beams through atmospheric turbulence.*”, *JOSA A* 31, 603–609, 2014.
- [67] Hamadou I., Roux F. S., McLaren M., Konrad T. and Forbes A. “*Orbital-angular-momentum entanglement in turbulence.*”, *Phys. Rev. A* 88, 012312, 2013.
- [68] Leonhard N., Sorelli G., Shatokhin V. N., Reinlein C. and Buchleitner A. “*Protecting the entanglement of twisted photons by adaptive optics.*”, *Phys. Rev. A* 97, 012321, 2018.
- [69] Roux F. S., Wellens T. and Shatokhin V. N. “*Entanglement evolution of twisted photons in strong atmospheric turbulence.*”, *Phys. Rev. A* 92, 012326, 2015.
- [70] Krenn M., Huber M., Fickler R., Lapkiewicz R., Ramelow S., and Zeilinger A. “*Generation and confirmation of a (100×100)-dimensional entangled quantum system.*”, *Proc. Natl. Acad. Sci. U.S.A.* 111, 6243, 2014.
- [71] Ferlic N. A., van Iersel M., Paulson D. A., and Davis C. C. “*Propagation of Laguerre-Gaussian and Im-Bessel beams through atmospheric turbulence: A computational study.*”, *Proc. SPIE 11506, Laser Communication and Propagation through the Atmosphere and Oceans IX*, 115060H, 2020.
- [72] Matsushima K. and Shimobaba T. “*Band-Limited Angular Spectrum Method for Numerical Simulation of Free-Space Propagation in Far and Near Fields.*”, *Opt. Express* 17, 19662-19673, 2009.

-
- [73] Zhang W., Zhang H. and Jin G. “*Band-extended angular spectrum method for accurate diffraction calculation in a wide propagation range.*”, *Opt. Lett.* 45, 1543-1546, 2020.
- [74] Zhang W., Zhang H. and Jin G. “*Single-Fourier transform based full-bandwidth Fresnel diffraction.*”, *J. Opt.* 23 035604, 2021.
- [75] Schmidt J. D. “*Numerical Simulation of Optical Wave Propagation with Examples in MATLAB.*”, *SPIE*, 2010.
- [76] Welsh B. M. “*A Fourier series based atmospheric phase screen generator for simulating anisoplanatic geometries and temporal evolution.*”, *Proc. SPIE*, 1997.
- [77] Lane R. G., Glindemann A. and Dainty J. C. “*Simulation of a Kolmogorov phase screen.*”, *Waves in Random Media*, 2, 1992.
- [78] Arrizón V., Ruiz U., Carrada R., and Gonzalez L. A. “*Pixelated phase computer holograms for the accurate encoding of scalar complex fields.*”, *J. Opt. Soc. Am. A* 24, 3500-3507, 2007.
- [79] Zhensong W., Shi Z., Liu Q. and Fu X. “*Holographic Tailoring of Structured Light Field with Digital Device.*”, *Photonics* 9, 7, 506, 2022
- [80] Nielsen M. A. and Chuang I. L. “*Quantum Computation and Quantum Information.*”, *Cambridge: Cambridge University Press*, 2000
- [81] Altepeter J.B., Jeffrey E.R., and Kwiat P.G. “*Photonic State Tomography.*”, *Advances In Atomic, Molecular, and Optical Physics*, Academic Press, 52, 2005.
- [82] James D. F. V., Kwiat P. G., Munro W. J., and White A. G. “*Measurement of qubits.*”, *Phys. Rev. A* 64, 052312, 2001.